

Using the Method of Moments and Robin Hood
Method to Solve Electromagnetic Scattering
Problems

by

David A. Chester

Submitted to the Department of Physics
in partial fulfillment of the requirements for the degree of

Bachelor of Science in Physics

at the

MASSACHUSETTS INSTITUTE OF TECHNOLOGY

June 2012

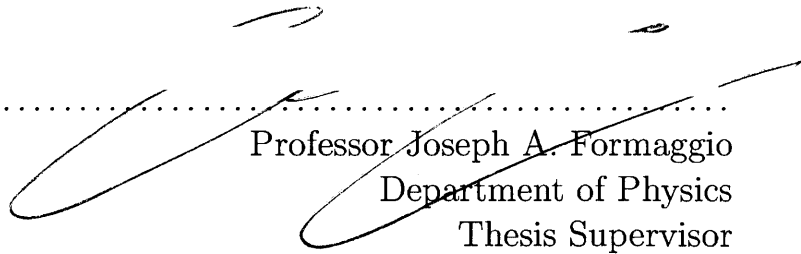
© Massachusetts Institute of Technology 2012. All rights reserved.



Author

Department of Physics
May 14, 2012

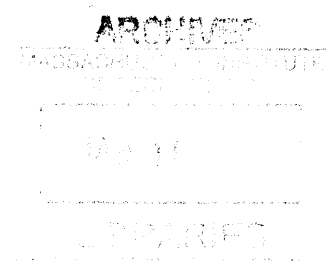
Certified by



Professor Joseph A. Formaggio
Department of Physics
Thesis Supervisor

Accepted by

Professor Nergis Mavalvala
Coordinator, Department of Physics



Using the Method of Moments and Robin Hood Method to Solve Electromagnetic Scattering Problems

by

David A. Chester

Submitted to the Department of Physics
on May 14, 2012, in partial fulfillment of the
requirements for the degree of
Bachelor of Science in Physics

Abstract

This thesis project was to write a program in C++ that solves electromagnetic scattering problems for arbitrarily shaped scatterers. This was implemented by using a surface integral formulation of Maxwell's equations, which discretizes the surface of the scatterer into thousands of triangles. The method of moments (MoM) was applied, which calculates the Green's functions between each triangle element. A matrix equation is obtained and solved using the Robin Hood (RH) method. The solution to this equation gives the scattered electromagnetic field. This program is first tested on a sphere, which is compared to the analytic solution known as Mie scattering. Once these results are confirmed, the program can be used for the KATRIN experiment to ensure that no Penning traps occur in the electron spectrometer.

Thesis Supervisor: Professor Joseph A. Formaggio
Title: Department of Physics

Acknowledgments

I would first like to thank my thesis advisor Prof. Joe Formaggio for giving me such a great research opportunity. He provided me with a challenging project which taught me details on electromagnetic scattering, numerical methods, and dynamic programming. I was given an independent project, but he was always there to assist me when I got stuck. Through these opportunities, I gained exposure to research in a new field. Also, Prof. Formaggio was always very friendly and kept my spirits up whenever I got discouraged.

I would also like to thank John Barrett, Richard Ott, Asher Kabolt, and Dr. Noah Oblath. They were always more than willing to help me out with any programming questions that I had. I started this project with no C++ experience, so they proved to be an invaluable resource. Whether it had to do with program organization, debugging, or understanding computer science concepts, they were always there to help.

Contents

1	Introduction	13
1.1	The KATRIN Experiment and Neutrino Mass Measurement	13
1.2	Thesis Outline	17
2	Electromagnetic Scattering Solutions and Motivation for the Method of Moments	19
2.1	Solving Maxwell's Equations	19
2.2	Numerical Method Classification and Brief Examples	20
2.2.1	Examples of Numerical Methods: FDTD, FEM, and MoM	21
2.2.2	Comparing Numerical Methods to Solve RF Scattering	23
3	Derivation of Surface Integral Equations and the Method of Moments	25
3.1	Surface Integral Equation Derivation from Maxwell's Equations	26
3.1.1	The Dyadic Green's Function and Dyadic Properties	28
3.1.2	Deriving the EFIE and MFIE	29
3.2	Including the Method of Moments to Solve the EFIE and MFIE	32
3.2.1	RWG Basis Functions	32
3.2.2	MoM Formulation to Give a Matrix Equation	33
4	Evaluating Dyadic Green's Functions and Surface Integrals	37
4.1	Singularity Subtraction of Green's functions	37
4.2	Calculating the Singular Part of Green's Functions	40

4.2.1	Calculation of Line and Surface Integrals	42
5	Using the Robin Hood Method to Solve Matrix Equations	47
5.1	Robin Hood Derivation for Electrostatic Problems	48
5.2	Robin Hood Applied to Electromagnetic Scattering Problems	50
6	Scattering by Spheres: Comparing RH and Mie Scattering	53
6.1	Implementation of Mie Scattering	53
6.1.1	Mie Scattering Equations	54
6.1.2	Implementing and Confirming Mie Scattering	56
6.2	Comparing MoM and RH to the Mie Solution	58
7	Future Work and Conclusions	61
7.1	Applying the MoM and RH to the Main Spectrometer	61
7.1.1	Simulating Penning Traps	61
7.1.2	Electron Cyclotron Resonance Simulations	63
7.2	Conclusions	65

List of Figures

1-1	Energy spectrum of electrons from tritium beta decay [1]. KATRIN only needs to accurately measure the electrons with the highest energy. The zoomed in portion gives models for the electron's energy spectrum if the neutrino had different mass values. Note that the endpoint is actually 18.575 keV, not 18.600 keV.	14
1-2	A layout of the KATRIN experiment.	15
3-1	Region 2 represents the scatterer, while region 1 represents the space surrounding the scatterer. S refers to the boundary of the surface between regions 1 and 2, while $\hat{\mathbf{n}}$ is the unit vector normal to the surface [2].	26
3-2	RWG basis functions: A basis is defined for each adjacent triangle edge n . T_n^+ and T_n^- are defined as the two triangles, where the currents flow from T_n^+ to T_n^- . The points $p_{1,n}$, $p_{2,n}$, p_n^+ , and p_n^- refer to the vertices of the triangles shown.	33
4-1	The coordinate system with three orthogonal vectors: $\hat{\mathbf{h}}$, $\hat{\mathbf{s}}$, and $\hat{\mathbf{t}}$. \mathbf{r}' represents a point along the edge of the two triangles and \mathbf{r} is on the triangles of the other edge [3].	43
4-2	The solid angle $d\Omega$ depends on the angle α , the normal vector $\hat{\mathbf{n}}$, and the vector $\mathbf{r} - \mathbf{r}'$	44

7-1	The left image shows how positive ions create electrons that do not re-enter the Penning trap. The right hand side shows the contrary effect [4].	63
7-2	The setup for ECR is displayed below. The frequency of the pulse generated must be tuned to be near the cyclotron frequency of the electrons in the Penning trap to ensure that they are excited [5]. . . .	64

List of Tables

6.1	This compares the results for the developed Mie scattering code with the work of Du, who matched the values of Wiscombe identically. Note that it only breaks down when the imaginary component of m_x is around 100. Besides those cases, the data agrees with the accepted values within 2 significant digits.	59
-----	--	----

Chapter 1

Introduction

1.1 The KATRIN Experiment and Neutrino Mass Measurement

This thesis project was to develop a program that calculates the scattered electromagnetic fields from arbitrary geometries. Numerical methods such as a surface integral formulation of Maxwell's equations, the method of moments, and the Robin Hood method are derived and explained. Once the numerical methods are implemented, Mie scattering is introduced, which scattering off a sphere. This provides an analytic comparison with the numerical methods to test against. Once confirmed, the numerical methods can be applied to calculate scattering for any shape. It is then used to understand the main spectrometer in the experiment KATRIN.

Observations such as neutrino oscillation suggest that neutrinos have a finite mass. KATRIN's goal is to measure the mass of the electron antineutrino. To do so, they measure the energy spectrum of electrons emitted from the beta decay of tritium. Tritium decays into helium-3, an electron, and an electron antineutrino. The neutrino only interacts through the weak force and gravity, so its presence cannot be detected. However, the neutrino's rest mass can be inferred if one accurately measures the electron's energy spectrum [6].

Fig. 1-1 illustrates the subtle effect of neutrino mass on the tritium beta decay

Figure 1-1: Energy spectrum of electrons from tritium beta decay [1]. KATRIN only needs to accurately measure the electrons with the highest energy. The zoomed in portion gives models for the electron's energy spectrum if the neutrino had different mass values. Note that the endpoint is actually 18.575 keV, not 18.600 keV.

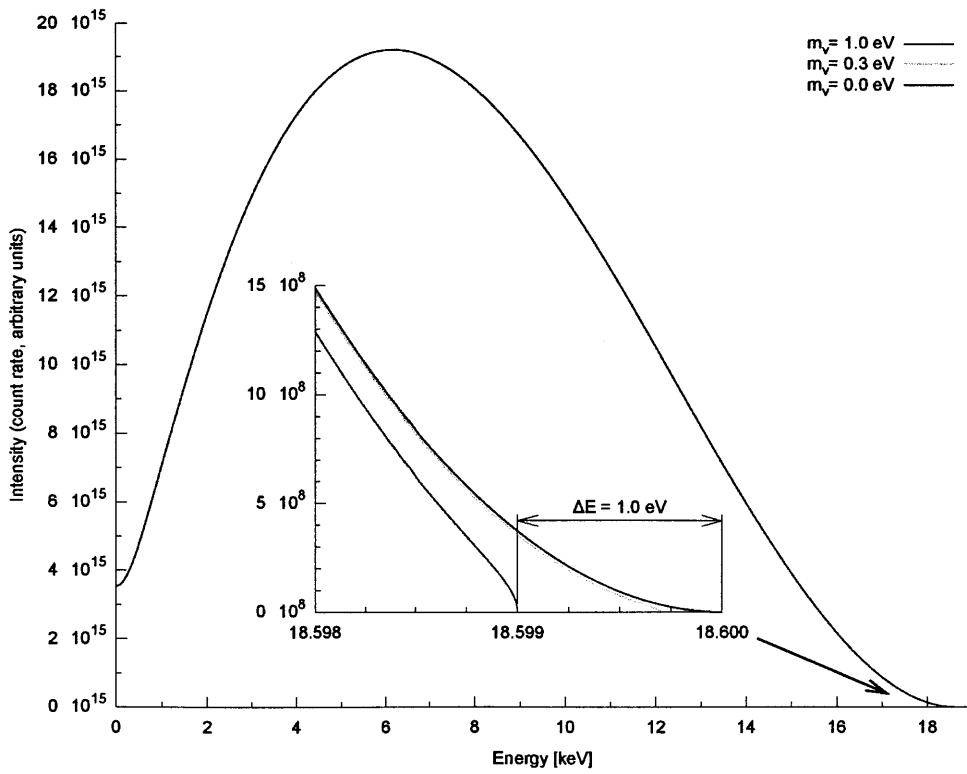
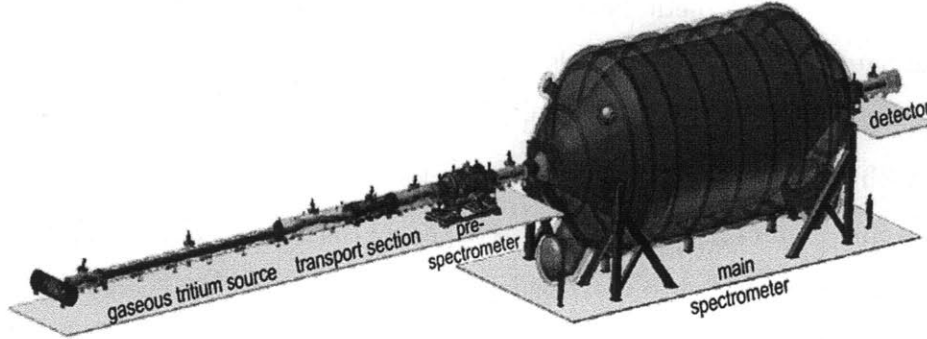


Figure 1-2: A layout of the KATRIN experiment.



spectrum. Most of the distortion occurs at the end of the spectrum. This is because the highest energy electrons correspond to neutrinos at rest. Therefore, only the most energetic electrons need to be measured.

The difficulty of this experiment comes from measuring the electron's energy with precision. Tritium beta decay properties tell us that the electron and antineutrino have a total energy of 18.6 keV. Analysis of various cosmological data such as measurements of the Lyman- α forest shows that the upper bound of the sum of the neutrino masses is 0.62 eV [7]. Since the antineutrino mass is such a small fraction of the total energy, it is imperative for KATRIN to have very accurate sensitivity in measuring the high energy electrons. KATRIN plans to reach a sensitivity of 0.2 eV at a 90% CL [8].

Fig. 1-2 shows the experimental design of KATRIN. The high luminosity gaseous tritium source provides 10^{11} beta decay electrons. The transport system has differential and cryogenic pumping sections to suppress the tritium flow. The electrons continue to travel through the pre-spectrometer and main spectrometer, which are described in detail below. The electrons are detected with a multi-pixel silicon semiconductor detector with ultra-high energy resolution.

The electron's energy spectrum is found using the two spectrometers. Both are

MAC-E-Filters (Magnetic Adiabatic Collimation with Electrostatic Filter). A retarding electrostatic potential is created, which only allows high energy electrons to enter the spectrometer. A magnetic field is produced by two superconduction solenoids, which collimates the electrons towards the detector.

The pre-spectrometer acts as a high energy pass filter by repelling most of the electrons with a fixed retarding voltage of 18.4 keV, just below the endpoint energy. This allows only 1 out of 10^7 of the electrons to pass to the main spectrometer. The low energy electrons are rejected to avoid pileup in the detector [9]. The energy spectrum of the electrons can be measured by varying the electrostatic potential. If the potential increases, less electrons will reach the detector and higher energy electrons will be measured. Varying this potential will give data for the energy spectrum. Carefully measuring the number of electrons detected at different potentials and comparing this data with Monte Carlo simulations determine the neutrino mass measurement [10].

Since KATRIN needs high energy resolution, the background must be well characterized. One source of background comes from Penning traps, which occur when charged particles get stuck in electromagnetic fields. The stuck electrons ionize the residual gas molecules, creating positively charged ions. These ions undergo further ionization processes with the gas which produce unwanted secondary electrons. If the positively charged ions are accelerated towards the detector, then the produced electrons will be detected and create a false signal. If they are not accelerated, then they stay trapped and produce more secondary electrons. Furthermore, photons can be created and produce secondary electrons, which build up exponentially [4]. Penning traps have been a problem in previous tritium decay experiments, such as Mainz [6].

To remove any electrons stuck in a Penning trap, an RF pulse is sent through the spectrometer. This excites the electrons into the walls of the spectrometer, which will not get detected. This process was successfully confirmed by simulations for the pre-spectrometer. However, modeling this effect with the main spectrometer is more challenging.

The research for this thesis project was initiated to simulate RF pulses in the main spectrometer. If the geometry of the spectrometer is discretized, numerical methods

can be utilized to calculate their response to incident RF pulses. These numerical simulation results can be compared to data experimentally obtained. It should be found that the actual RF responses agree with simulations. This thesis derives the numerical methods used to solve general electromagnetic scattering problems. While the simulation is being used specifically for KATRIN, these methods are applicable to a variety of applications.

1.2 Thesis Outline

Chapter 2 introduces Maxwell's equations and electromagnetic scattering theory. It describes why numerical methods must be utilized to solve complicated systems and outlines popular numerical techniques for solving electromagnetic problems. Furthermore, it provides the motivation for the method of moments and surface integral equation formulations.

Chapter 3 derives surface integral equations from Maxwell's equations. This formulation requires Green's functions to be calculated between each discretized element. Applying the method of moments allows for the solution to be expanded in terms of these elements and provides the basis used for obtaining a matrix equation.

Chapter 4 describes how the Green's functions and surface integrals are calculated. Since there are singular portions in the matrix elements, a singularity subtraction method is introduced. This allows for a closed form solution to the singular part of the Green's functions, which can be subtracted to allow numerical integration and then added back later.

Chapter 5 explains how the matrix equation is solved using the Robin Hood algorithm, which had previously only been applied to static cases. RH is first outlined for the simpler electrostatic case. Then, it is described how it is altered to be applied to the derived surface integral formulation.

Chapter 6 introduces Mie scattering, which analytically calculates electromagnetic scattering for spheres. The technique for solving Mie scattering is provided and compared to previous Mie scattering calculations. From there, it can be compared to

the numerical methods developed, to ensure that RH is properly solving the surface integral equations.

Chapter 7 discusses how the electromagnetic solver will be applied to the main spectrometer in KATRIN to solve RF problems. Also, concluding remarks and future research plans will be given.

Chapter 2

Electromagnetic Scattering

Solutions and Motivation for the Method of Moments

2.1 Solving Maxwell's Equations

Maxwell's equations are a series of partial differential equations which relate electric and magnetic fields to charges and currents. In principle, they exactly describe any electromagnetic interaction. While these equations were first written down in 1861, new approaches for finding solutions are still being developed today. In principle, one could find a unique solution given initial and boundary conditions, but many systems do not have analytic solutions. Analytic methods provide exact solutions which can be found from mathematical manipulations. These include introductory electromagnetism problems, such as calculating the electric field due to a charged sphere, cylinder, or infinite plane.

Consider the scattering of light on matter for example. Analytic solutions only exist in systems with great symmetry, such as the sphere. Mie scattering is the solution that describes light scattering off of a homogenous sphere. Even these analytic solutions must be expressed in terms of an infinite series. The Mie solution can be

expanded to describe multiple spheres, coated spheres, spheroids, and infinite cylinders. A derivation of the Mie solution is presented in Chapter 6. Unfortunately, there are no analytic solutions for more complex scatterers.

It is unlikely that any new analytic methods will be found for electromagnetism problems. However, numerical methods are still being developed to provide approximate solutions. Numerical methods find field values at specific discrete points, rather than continuously as analytic methods do. Fortunately, computers are well suited for iterative numerical techniques and can handle complex discretization schemes.

There are multiple terms to characterize the success of each numerical method. Ideally, the best method calculates an approximate solution closest to the exact solution in the shortest amount of computational time. To determine the accuracy of a method, the system can be simplified and compared to an available analytic solution. If the method is found to be accurate, then it should apply to more complex systems as well. A scheme is said to be stable if there are no numerical or round-off errors. Convergence means that if the discretization length was set to zero, then the numerical solution approaches the exact solution. Efficiency refers to how fast a method determines a solution [11].

These terms can be used to discuss the advantages and disadvantages of different methods in specific cases. For example, one may start by choosing the most efficient method, but then realize that it does not give an accurate enough result. Another method may not converge in all of the regimes needed.

2.2 Numerical Method Classification and Brief Examples

In general, numerical methods can be used to solve any boundary value problem, which are differential equations with a set of boundary conditions. While many numerical methods are similar and can be difficult to classify, they can be broken into two groups: differential and integral methods. Since there are differential and integral

forms of Maxwell's equations, both techniques can be used to solve electromagnetic problems.

2.2.1 Examples of Numerical Methods: FDTD, FEM, and MoM

Typically, partial differential equations (PDEs) which describe the boundary value problem are converted into difference equations which can be solved by iterative methods. Differential methods typically make approximations to replace the differential operators.

The first and simplest numerical method ever constructed was the finite difference method (FDM). When it is applied to electromagnetism, it is known as the finite-difference time-domain (FDTD). It approximates the differential operators in the partial differential equations [12]. For example, the first order derivative of a scalar potential ϕ would have the following approximation:

$$\frac{d\phi}{dx}(a) \approx \frac{\phi(a+h) - \phi(a)}{h}. \quad (2.1)$$

This is an example of the simplest FDM. However, most partial differential equations contain more complicated differential operators, often second order derivatives. By approximations, such as Taylor expansions, higher order operators can be approximated as well. These methods are relatively simple, but are not always useful because an orthogonal discretization grid must be applied to space of interest. This is not particularly useful for systems with curvilinear boundaries. Also, Maxwell's equations in their differential form do not hold on boundaries, so neither do their approximations [13].

The finite element method (FEM) is a variational approach where the PDE is converted into a functional. It can be used on differential and integral equations, but is most commonly used for differential equations. The solution is approximated by breaking it up into multiple bases, and each basis function is given a weight. From here, a matrix equation can be solved in terms of these bases to obtain a solution

[12][14]. Similar to FDM, FEM discretizes the fields throughout all of space. The functional is then minimized by guessing different weights, which determines the approximate solution.

One advantage of integral methods is that only the scatterer needs to be discretized, rather than all of space. The method of moments (MoM) is an example of an integral equation method, which is closely related to the boundary element method (BEM). It is similar to FEM in that it expands the solution in terms of basis functions. The difference is that each matrix element is calculated by performing an integral equation involving the Green's functions between each basis [12].

The MoM reduces an integral equation into a matrix equation. Let's assume we have $Lf = g$, where L is a linear operator, f is the solution to be determined, and g is the source. Expand f as a series of functions: $f = \sum_n \alpha_n f_n$. Let each f_n be known as basis functions. The solutions that are found for electromagnetism problems would be the current and charge distributions. Typically, an exact solution would require an infinite number of basis functions, but an approximate solution utilizes a finite number. From here, we have $\sum_n \alpha_n Lf_n = g$. Most generally, weighting functions w_m can be introduced and the inner product of these weighting functions and each side of the equation is performed. This gives a matrix equation of the following form: $\sum_n \alpha_n \langle w_m, Lf_n \rangle = \langle w_m, g \rangle$, where $\langle a, b \rangle$ represents the inner product of a and b . The matrix equation is more clearly seen making the following redefinitions:

$$I_{mn}\alpha_n = g_m, \text{ where} \tag{2.2}$$

$$I_{mn} = \begin{pmatrix} \langle w_1, Lf_1 \rangle & \langle w_1, Lf_2 \rangle & \dots \\ \langle w_2, Lf_1 \rangle & \langle w_2, Lf_2 \rangle & \dots \\ \vdots & \vdots & \ddots \end{pmatrix}, \tag{2.3}$$

$$\alpha_n = \begin{pmatrix} \alpha_1 \\ \alpha_2 \\ \vdots \end{pmatrix}, \text{ and } w_m = \begin{pmatrix} w_1 \\ w_2 \\ \vdots \end{pmatrix}. \tag{2.4}$$

The weighted functions w_n must be chosen. Galerkin's method is to choose $w_n =$

f_n . From here, the solution can be found if the matrix I_{mn} is invertible. The MoM is very powerful, but can only be used if there are known Green's functions for the studied equation [15].

2.2.2 Comparing Numerical Methods to Solve RF Scattering

Differential equation formulations are often straightforward and can be used to solve most problems. However, a mesh must be created for the scatterer and the surrounding space. If the geometry of the scatterer is a complicated 3D structure, the mesh must match this accurately, which can be time consuming. Also, if the boundary conditions of the fields are set at infinity, the space must be truncated to become finite. This introduces unnecessary error into the boundary conditions themselves. For the FDTD, both space and time must be discretized, since the spatial and temporal derivatives must be replaced by difference quantities.

Integral equation formulations only discretize the scatterer, but often have higher memory costs. It can be more difficult to calculate fields with IEs, but they tend to deal with complex geometries better, because only the scatterer needs to be discretized. Also, boundary conditions at infinity can be accounted for. The MoM is very accurate because the derived equations are almost exact. It is very applicable for complex scatterers because it works with surface or volume discretizations of any manner [16].

There are surface integral equation (SIE) and volume integral equation (VIE) formulations [17]. While VIEs are easily obtained from Maxwell's equations, SIEs tend to use less memory. This is because the number of discretizations needed for a surface scales with the second power of the radius, while the number of volume discretizations scales with the third power of the radius. VIEs only slowly improve their accuracy as discretization increases. VIEs are more versatile because they are applicable to inhomogeneous scatterers, while SIEs can only be used for homogeneous scatterers [2][12].

Chapter 3

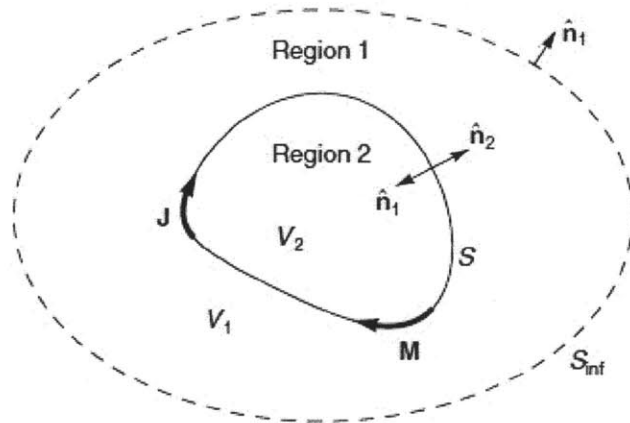
Derivation of Surface Integral Equations and the Method of Moments

The previous chapter motivated that integral techniques are useful for electromagnetic scattering problems because only the scatterer needs to be discretized. If the scatterer is homogeneous, then SIEs can be employed and require less memory allocation than VIEs. Since Green's functions can be found, the MoM can be applied to achieve accurate solutions.

Before diving into derivation, the problem will be clearly defined. Consider some arbitrary homogeneous 3D geometry, as shown in Fig. 3-1. Homogeneous states that the scatterer has a constant refractive index. Maxwell's equations will be solved in two regions. Region 1 represents the space around the geometry, and region 2 is the geometry itself. Given an incident electromagnetic wave of a specific frequency, the scattered electromagnetic waves are to be calculated.

To approach this problem numerically, surface integral equations will be derived from Maxwell's equations. Next, the surface of the geometry is discretized into many triangles. The solution of surface currents is expanded into a set of RWG functions. Finally, the weighted coefficient for each RWG function is solved by inverting the matrix by the Robin Hood method (RH). This chapter focuses on deriving the surface

Figure 3-1: Region 2 represents the scatterer, while region 1 represents the space surrounding the scatterer. S refers to the boundary of the surface between regions 1 and 2, while \hat{n} is the unit vector normal to the surface [2].



integral equations and introduces the matrix equation to be solved.

3.1 Surface Integral Equation Derivation from Maxwell's Equations

To derive the needed surface integral equations, Maxwell's equations will be manipulated to form electric and magnetic wave equations. From there, a dyadic Green's function is introduced to generate fields from sources. Next, the electric field integral equation (EFIE) and magnetic field integral equation (MFIE) can be derived. Once these equations are found, the MoM is applied to give bases for defining a matrix equation. The EFIE and MFIE are then combined into a new matrix equation, which can be solved to give the scattered fields. The derivation of this matrix equation starts below.

Here are Maxwell's equations in differential form using SI units:

$$\nabla \times \mathbf{H}(\mathbf{r}, t) = \mathbf{j}_f(\mathbf{r}, t) + \frac{\partial \mathbf{D}(\mathbf{r}, t)}{\partial t}, \quad (3.1)$$

$$\nabla \times \mathbf{E}(\mathbf{r}, t) = -\frac{\partial \mathbf{B}(\mathbf{r}, t)}{\partial t}, \quad (3.2)$$

$$\nabla \cdot \mathbf{B}(\mathbf{r}, t) = 0, \quad (3.3)$$

$$\nabla \cdot \mathbf{D}(\mathbf{r}, t) = \rho_f(\mathbf{r}, t), \quad (3.4)$$

where \mathbf{H} is the magnetic field, \mathbf{E} is the electric field, \mathbf{B} is the magnetic flux density, \mathbf{D} is the electric flux density, \mathbf{j}_f is the free current density, ρ_f is the free charge density, and c is the speed of light. If we assume there are no bound charges or currents, then $\mathbf{D} = \varepsilon(\mathbf{r})\mathbf{E}$ and $\mathbf{B} = \mu(\mathbf{r})\mathbf{H}$, where $\varepsilon(\mathbf{r})$ is the electric permittivity and $\mu(\mathbf{r})$ is the magnetic permeability. In region 1, $\varepsilon(\mathbf{r}) = \varepsilon_0$ and $\mu(\mathbf{r}) = \mu_0$, since it is empty space. Since a homogeneous scatterer was assumed, region 2 has spatially independent values for ε and μ .

Taking a time derivative of (3.1), plugging it into (3.2), and taking a curl of both sides gives the following wave equation for the electric field:

$$\nabla \times \nabla \times \mathbf{E}(\mathbf{r}, t) + \frac{\varepsilon(\mathbf{r})\mu(\mathbf{r})}{c^2} \frac{\partial^2 \mathbf{E}(\mathbf{r}, t)}{\partial t^2} = -\mu(\mathbf{r}) \frac{\partial \mathbf{j}(\mathbf{r}, t)}{\partial t}. \quad (3.5)$$

Next, a time-harmonic electric field is assumed, giving $\mathbf{E}(\mathbf{r}, t) = \exp(-i\omega t)\mathbf{E}(\mathbf{r})$. The current density also is assumed to be time-harmonic. This allows the time derivatives to be evaluated, giving

$$\nabla \times \nabla \times \mathbf{E}(\mathbf{r}) - \frac{\omega^2}{c^2} \varepsilon(\mathbf{r})\mu(\mathbf{r})\mathbf{E}(\mathbf{r}) = i\omega\mu\mathbf{j}(\mathbf{r}). \quad (3.6)$$

This is known as the vector Helmholtz equation [18]. Assuming a time-harmonic field constrains this approach to be a frequency-based method, rather than a time-based method. This method only calculates electromagnetic scattering for a specific frequency. Time-based methods require time to be discretized as well. However, if one wants to calculate broad frequency spectrum scattering effects, this method must

be implemented multiple times for each frequency.

Similar manipulations can be done to obtain a magnetic wave equation. Noting the wavenumber, $k = \omega(\varepsilon\mu)^{1/2}$, and adding an index i to represent the two different regions, the following electric and magnetic wave equations are obtained:

$$\nabla \times \nabla \times \mathbf{E}_i(\mathbf{r}) - k_i^2 \mathbf{E}_i(\mathbf{r}) = i\omega\mu_i \mathbf{j}(\mathbf{r}), \quad \mathbf{r} \in V_i, \quad (3.7)$$

$$\nabla \times \nabla \times \mathbf{H}_i(\mathbf{r}) - k_i^2 \mathbf{H}_i(\mathbf{r}) = \nabla \times \mathbf{j}(\mathbf{r}), \quad \mathbf{r} \in V_i. \quad (3.8)$$

3.1.1 The Dyadic Green's Function and Dyadic Properties

Next, the dyadic Green's function $\bar{\mathbf{G}}(\mathbf{r}, \mathbf{r}')$ is introduced. A dyadic is similar to a matrix, since this is made up of three vectors containing Green's functions. There is no distinction on the difference between a row and a column for dyadics. Letting the electric field have the following definition in terms of the dyadic Green's function,

$$\mathbf{E}_i(\mathbf{r}) = i\omega\mu_i \int_V d\mathbf{r}' \mathbf{j}(\mathbf{r}') \cdot \bar{\mathbf{G}}_i(\mathbf{r}', \mathbf{r}). \quad (3.9)$$

This equation physically shows that a dyadic Green's function operating on an electric current generates the corresponding electric field. It is no surprise that plugging this into the previous wave equation gives a differential equation with a delta function:

$$\nabla \times \nabla \times \bar{\mathbf{G}}_i(\mathbf{r}, \mathbf{r}') - k_i^2 \bar{\mathbf{G}}_i(\mathbf{r}, \mathbf{r}') = \bar{\mathbf{I}} \delta(\mathbf{r} - \mathbf{r}'), \quad (3.10)$$

where $(\bar{\mathbf{I}})_{ij} = \delta_{ij}$. A solution for the dyadic Green's function can be found to have the following form:

$$\bar{\mathbf{G}}_i(\mathbf{r}, \mathbf{r}') = \left(\bar{\mathbf{I}} + \frac{\nabla \nabla}{k_i^2} \right) \frac{e^{ik_i R}}{4\pi R}, \quad (3.11)$$

where $R = |\mathbf{r} - \mathbf{r}'|$. Note that the scalar free-space Green's function, $G_i(\mathbf{r}, \mathbf{r}') = \frac{e^{ik_i R}}{4\pi R}$, is embedded in the dyadic Green's function [19].

Ref. [20] has extensive explanation on the properties of a dyadic. The following properties will be used for this derivation. Dyadic analysis shows that the anterior and posterior dot products can be defined for a vector \mathbf{a} and dyadic $\bar{\mathbf{M}}$, which are

written as $\mathbf{a} \cdot \bar{\mathbf{M}}$ and $\bar{\mathbf{M}} \cdot \mathbf{a}$, respectively. This returns a vector quantity, and the two are related by $\mathbf{a} \cdot \bar{\mathbf{M}}^T = \bar{\mathbf{M}} \cdot \mathbf{a}$. Furthermore, the anterior and posterior cross products, $\mathbf{a} \times \bar{\mathbf{M}}$ and $\bar{\mathbf{M}} \times \mathbf{a}$, return dyadics. For vectors \mathbf{a} , \mathbf{b} , and dyadic $\bar{\mathbf{C}}$,

$$\mathbf{a} \cdot (\mathbf{b} \times \bar{\mathbf{C}}) = -\mathbf{b} \cdot (\mathbf{a} \times \bar{\mathbf{C}}) = (\mathbf{a} \times \mathbf{b}) \cdot \bar{\mathbf{C}}, \quad (3.12)$$

which is an abstraction from the corresponding vector identity. The reciprocity theorem gives $\bar{\mathbf{G}}^T(\mathbf{r}, \mathbf{r}') = \bar{\mathbf{G}}(\mathbf{r}', \mathbf{r})$ and $(\nabla \times \bar{\mathbf{G}}(\mathbf{r}, \mathbf{r}'))^T = -\nabla \times \bar{\mathbf{G}}(\mathbf{r}', \mathbf{r})$ [21].

3.1.2 Deriving the EFIE and MFIE

Now that the needed properties of a dyadic are given, surface integral equations can be derived in terms of the Green's functions and the fields, which correspond to the EFIE and MFIE.

Taking the anterior product of Eq. (3.7) with $\bar{\mathbf{G}}_i(\mathbf{r}, \mathbf{r}')$, the anterior product of $\mathbf{E}_i(\mathbf{r})$ with Eq. (3.10), and subtracting these two equations gives

$$\begin{aligned} \nabla \times \nabla \times \mathbf{E}_i(\mathbf{r}) \cdot \bar{\mathbf{G}}_i(\mathbf{r}, \mathbf{r}') - \mathbf{E}_i(\mathbf{r}) \cdot \nabla \times \nabla \times \bar{\mathbf{G}}_i(\mathbf{r}, \mathbf{r}') \\ = i\omega\mu_i \mathbf{j}(\mathbf{r}) \cdot \bar{\mathbf{G}}_i(\mathbf{r}, \mathbf{r}') - \mathbf{E}_i(\mathbf{r}) \delta(\mathbf{r} - \mathbf{r}'). \end{aligned} \quad (3.13)$$

Using Eq.(3.12) on the first and second terms in the left-hand side of Eq. (3.13) and taking a volume integral gives

$$\begin{aligned} \int_{V_i} dV \nabla \cdot ([\nabla \times \mathbf{E}_i(\mathbf{r})] \times \bar{\mathbf{G}}_i(\mathbf{r}, \mathbf{r}') + \mathbf{E}_i(\mathbf{r}) \times [\nabla \times \bar{\mathbf{G}}_i(\mathbf{r}, \mathbf{r}')] \\ = i\omega\mu_i \int_{V_i} dV \mathbf{j}(\mathbf{r}) \cdot \bar{\mathbf{G}}_i(\mathbf{r}, \mathbf{r}') - \begin{cases} \mathbf{E}_i(\mathbf{r}') : & \mathbf{r}' \in V_i \\ 0 : & \text{otherwise} \end{cases}. \end{aligned} \quad (3.14)$$

Using Eq. (3.9) allows a simplification of the right-hand side of Eq. (3.14), allowing the first term to represent the incident electric field $\mathbf{E}_i^{inc}(\mathbf{r}')$. Eq. (A.45) in [20] gives a vector-dyadic Green's theorem converting volume integrals into surface integrals, which can be applied to the left-hand side of Eq. (3.14). Applying these two changes

gives

$$\int_{\partial V_i} dS \hat{\mathbf{n}}_i(\mathbf{r}) \cdot ([\nabla \times \mathbf{E}_i(\mathbf{r})] \times \bar{\mathbf{G}}_i(\mathbf{r}, \mathbf{r}') + \mathbf{E}_i(\mathbf{r}) \times [\nabla \times \bar{\mathbf{G}}_i(\mathbf{r}, \mathbf{r}')]) = \mathbf{E}_i^{inc}(\mathbf{r}'), \quad (3.15)$$

where ∂V_i represents the boundary surface of V_i and $\hat{\mathbf{n}}_i$ is the outward pointing normal vector of that surface. In other words, $\partial V_2 = S$ and $\partial V_1 = S_{inf} \cup (-S)$. The first term of the left-hand side of this equation can be further simplified by using Eq. (3.12), Eq. (3.2) assuming time-harmonic fields, and reciprocity, which gives

$$\begin{aligned} \hat{\mathbf{n}}_i(\mathbf{r}) \cdot [\nabla \times \mathbf{E}_i(\mathbf{r})] \times \bar{\mathbf{G}}_i(\mathbf{r}, \mathbf{r}') &= \hat{\mathbf{n}}_i(\mathbf{r}) \times [\nabla \times \mathbf{E}_i(\mathbf{r})] \cdot \bar{\mathbf{G}}_i(\mathbf{r}, \mathbf{r}') \\ &= i\omega\mu_i \bar{\mathbf{G}}_i(\mathbf{r}', \mathbf{r}) \cdot [\hat{\mathbf{n}}_i(\mathbf{r}) \times \mathbf{H}_i(\mathbf{r})]. \end{aligned} \quad (3.16)$$

The second term of Eq. (3.15) can be simplified by Eq. (3.12) and reciprocity, giving

$$\begin{aligned} \hat{\mathbf{n}}(\mathbf{r}) \cdot \mathbf{E}_i(\mathbf{r}) \times [\nabla \times \bar{\mathbf{G}}_i(\mathbf{r}, \mathbf{r}')] &= [\hat{\mathbf{n}}(\mathbf{r}) \times \mathbf{E}_i(\mathbf{r})] \cdot [\nabla \times \bar{\mathbf{G}}_i(\mathbf{r}, \mathbf{r}')] \\ &= -[\nabla \times \bar{\mathbf{G}}_i(\mathbf{r}', \mathbf{r})] \cdot [\hat{\mathbf{n}}(\mathbf{r}) \times \mathbf{E}_i(\mathbf{r})]. \end{aligned} \quad (3.17)$$

Now, it is convenient to introduce the electric and magnetic surface current densities $\mathbf{J} = \hat{\mathbf{n}}_2 \times \mathbf{H}_i$ and $\mathbf{M} = -\hat{\mathbf{n}}_2 \times \mathbf{E}_i$. When the MoM is performed, \mathbf{J} and \mathbf{M} are the solutions that will be found. Assuming that region 2 is nonemitting gives $\mathbf{j} = 0$ in V_2 , which means $\mathbf{E}_2^{inc} = 0$. Introducing the surface current densities, simplifying the right-hand side, and switching \mathbf{r} and \mathbf{r}' gives

$$\begin{aligned} \frac{\omega\mu_i}{i} \int_S dS' \bar{\mathbf{G}}_i(\mathbf{r}, \mathbf{r}') \cdot \mathbf{J}(\mathbf{r}') - \int_S dS' [\nabla' \times \bar{\mathbf{G}}_i(\mathbf{r}, \mathbf{r}')] \cdot \mathbf{M}(\mathbf{r}') \\ = \begin{cases} \mathbf{E}_1^{inc}(\mathbf{r}) : & i = 1 \text{ and } \mathbf{r} \in V_2 \setminus S \\ 0 : & i = 2 \text{ and } \mathbf{r} \in V_1 \setminus S \end{cases} \end{aligned} \quad (3.18)$$

Note that the same \mathbf{J} and \mathbf{M} are used for both regions. This combined with the fact

that $\hat{\mathbf{n}}_1 = -\hat{\mathbf{n}}_2$ gives the following boundary conditions

$$\hat{\mathbf{n}}_i \times (\mathbf{E}_1(\mathbf{r}) - \mathbf{E}_2(\mathbf{r})) \quad (3.19)$$

$$\hat{\mathbf{n}}_i \times (\mathbf{H}_1(\mathbf{r}) - \mathbf{H}_2(\mathbf{r})). \quad (3.20)$$

These boundary conditions state that the tangential component of the electric and magnetic fields are continuous across the boundary S . Since this is true, one can take the limit of $\mathbf{r} \rightarrow S$ for Eq. (3.18). Doing so gives the desired EFIE

$$\begin{aligned} & \left(\frac{\omega\mu_i}{i} \int_S dS' \bar{\mathbf{G}}_i(\mathbf{r}, \mathbf{r}') \cdot \mathbf{J}(\mathbf{r}') - \int_S dS' [\nabla' \bar{\mathbf{G}}_i(\mathbf{r}, \mathbf{r}')] \cdot \mathbf{M}(\mathbf{r}') \right)_{tan} \\ & = \begin{cases} (\mathbf{E}_1^{inc}(\mathbf{r}))_{tan} : & i = 1 \\ 0 : & i = 2 \end{cases}, \end{aligned} \quad (3.21)$$

for $\mathbf{r} \in S$.

Similar manipulations can be done to Eq. (3.8) instead of Eq. (3.7), which gives the MFIE. First, the incident magnetic must be generated by the following, which is analogous to Eq. (3.9)

$$\mathbf{H}_i^{inc}(\mathbf{r}') = \int_{V_i} dV [\nabla' \times \mathbf{j}(\mathbf{r})] \cdot \bar{\mathbf{G}}_i(\mathbf{r}, \mathbf{r}'). \quad (3.22)$$

Using this field generating equation and similar manipulations that obtained the EFIE, the MFIE is found to have the following form

$$\begin{aligned} & \left(\frac{\omega\epsilon_i}{i} \int_S dS' \bar{\mathbf{G}}_i(\mathbf{r}, \mathbf{r}') \cdot \mathbf{M}(\mathbf{r}') + \int_S dS' [\nabla' \bar{\mathbf{G}}_i(\mathbf{r}, \mathbf{r}')] \cdot \mathbf{J}(\mathbf{r}') \right)_{tan} \\ & = \begin{cases} (\mathbf{H}_1^{inc}(\mathbf{r}))_{tan} : & i = 1 \\ 0 : & i = 2 \end{cases}, \end{aligned} \quad (3.23)$$

for $\mathbf{r} \in S$.

These EFIE and MFIE contain exactly what was desired [2]. They are surface integral equations including the dyadic Green's function, the electric and magnetic surface currents as a solution, and the incident fields as a source. Note that no

approximations have been made yet, making these equations exact. Next, a method to solve these equations is needed.

3.2 Including the Method of Moments to Solve the EFIE and MFIE

The MoM is the numerical technique to be used to solve for electromagnetic scattering. The goal is to find solutions for \mathbf{J} and \mathbf{M} . From there, the scattered electric and magnetic fields can be found. Since Eqs. (3.23) and (3.21) are surface integral equations, it is intuitive to discretize the surface of S . The surface will be broken into triangles, since they are simple and effective. Chapter 2 showed that the MoM expands the solution in terms of basis functions. The most common basis functions for triangles are RWG functions, which will be used to expand the solution and apply the MoM.

3.2.1 RWG Basis Functions

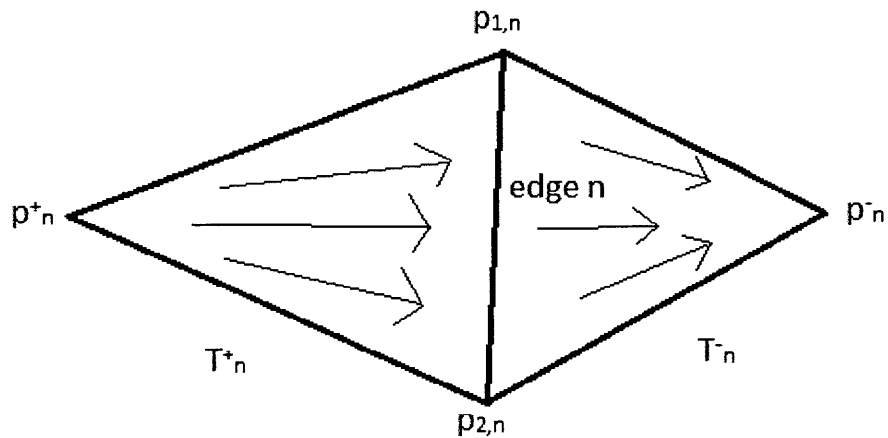
Once the surface is broken into triangles, RWG basis functions can be found for each shared edge between two triangles, as shown in Fig. 3-2. For a common edge n , there are two adjacent triangles T_n^+ and T_n^- . The determination of which triangle is plus or minus is determined by which direction is considered a positive current, so the choice is arbitrary.

Since the electric and magnetic surface densities are vector quantities, one must expand with a vector function. The RWG basis function takes the following form

$$\mathbf{f}_n(\mathbf{r}) = \begin{cases} \pm \frac{L_n}{2A_n^\pm}(\mathbf{r} - \mathbf{p}_n^\pm) : & \mathbf{r} \in T_n^\pm \\ 0 : & \text{otherwise} \end{cases}, \quad (3.24)$$

where L_n is the length of the common edge n , A_n^\pm is the area of T_n^\pm , and \mathbf{p}_n^\pm is the third point of T_n^\pm not connected to the common edge. It will also be useful to note

Figure 3-2: RWG basis functions: A basis is defined for each adjacent triangle edge n . T_n^+ and T_n^- are defined as the two triangles, where the currents flow from T_n^+ to T_n^- . The points $p_{1,n}$, $p_{2,n}$, p_n^+ , and p_n^- refer to the vertices of the triangles shown.



the divergence of the RWG basis function [22]

$$\nabla \cdot \mathbf{f}_n(\mathbf{r}) = \begin{cases} \pm \frac{L_n}{A_n} : & \mathbf{r} \in T_n^\pm \\ 0 : & \text{otherwise} \end{cases} \quad (3.25)$$

Now that the basis functions are stated, the solution can be expanded to apply the MoM.

3.2.2 MoM Formulation to Give a Matrix Equation

Expanding in terms of basis functions, the electric and magnetic surface current densities are approximated by

$$\mathbf{J}(\mathbf{r}) = \sum_{n=1}^N \alpha_n \mathbf{f}_n(\mathbf{r}), \quad (3.26)$$

$$\mathbf{M}(\mathbf{r}) = \sum_{n=1}^N \beta_n \mathbf{f}_n(\mathbf{r}), \quad (3.27)$$

where N is the total number of edges. α_n and β_n are now the solution coefficients to be found. Galerkin's method of weighted residuals uses the same basis functions to

test the EFIE, Eq. (3.21), and the MFIE, Eq. (3.23). Applying this approximation changes the EFIE to

$$\begin{aligned} \int_{S_m} dS \mathbf{f}_m(\mathbf{r}) \cdot \sum_{n=1}^N \left(\alpha_n \frac{\omega \mu_i}{i} \int_{S_n} dS' \bar{\mathbf{G}}_i(\mathbf{r}, \mathbf{r}') \cdot \mathbf{f}_n(\mathbf{r}') - \beta_n \int_{S_n} dS' [\nabla' \times \bar{\mathbf{G}}_i(\mathbf{r}, \mathbf{r}')] \cdot \mathbf{f}_n(\mathbf{r}') \right) \\ = \begin{cases} \int_{S_m} dS \mathbf{f}_m(\mathbf{r}) \cdot \mathbf{E}_1^{inc}(\mathbf{r}) : & i = 1 \\ 0 : & i = 2 \end{cases}, \end{aligned} \quad (3.28)$$

for $m = 1 \dots N$, where S_m includes T_m^+ and T_m^- . Adding these basis functions allows for the construction of the matrix equation,

$$\begin{bmatrix} \mathbf{D}^1 & -\mathbf{K}^1 \\ \mathbf{D}^2 & -\mathbf{K}^2 \end{bmatrix} \boldsymbol{\psi} = \mathbf{q}^E, \quad (3.29)$$

where \mathbf{D}^i and \mathbf{K}^i are submatrices defined as

$$\mathbf{D}_{mn}^i = \frac{\omega \mu_i}{i} \int_{S_m} dS \mathbf{f}_m(\mathbf{r}) \cdot \int_{S_n} dS' \bar{\mathbf{G}}_i(\mathbf{r}, \mathbf{r}') \cdot \mathbf{f}_n(\mathbf{r}'), \quad (3.30)$$

$$\mathbf{K}_{mn}^i = \int_{S_m} dS \mathbf{f}_m(\mathbf{r}) \cdot \int_{S_n} dS' [\nabla' \times \bar{\mathbf{G}}_i(\mathbf{r}, \mathbf{r}')] \cdot \mathbf{f}_n(\mathbf{r}'), \quad (3.31)$$

where $m, n = 1 \dots N$. The vector quantity solution is

$$\boldsymbol{\psi} = (\alpha_1, \dots, \alpha_N, \beta_1, \dots, \beta_N)^T, \quad (3.32)$$

and the vector quantity of initial conditions is

$$\mathbf{q}_m^E = \begin{cases} \int_{S_m} dS \mathbf{f}_m(\mathbf{r}) \cdot \mathbf{E}_1^{inc}(\mathbf{r}) : & m = 1 \dots N \\ 0 : & m = N + 1 \dots 2N \end{cases}. \quad (3.33)$$

In the matrix equation (3.29), the matrix contains all of the information from the Green's functions. Each element of \mathbf{D}_{mn}^i gives a correlation between the two edges m and n . \mathbf{q}^E gives the initial conditions for the system, which is the incident electric field at each edge. Assuming the Green's functions can be evaluated analytically, the

solution $\boldsymbol{\psi}$ can be found, which has the coefficients needed to find the surface current densities on each edge. The scattered electric field then can be calculated from the surface current densities.

A similar matrix equation can be found for the MFIE,

$$\begin{bmatrix} \mathbf{K}^1 & \frac{\mathbf{D}^1}{Z_1^2} \\ \mathbf{K}^2 & \frac{\mathbf{D}^2}{Z_2^2} \end{bmatrix} \boldsymbol{\psi} = \mathbf{q}^H, \quad (3.34)$$

where $Z_i = \sqrt{\mu_i \varepsilon_i}$, and \mathbf{q}^H contains the incident magnetic field

$$\mathbf{q}_m^H = \begin{cases} \int_{S_m} dS \mathbf{f}_m(\mathbf{r}) \cdot \mathbf{H}_1^{inc}(\mathbf{r}) : & m = 1 \dots N \\ 0 : & m = N + 1 \dots 2N \end{cases}. \quad (3.35)$$

Currently, the EFIE and MFIE solve for the same coefficients due to an incident electric or magnetic field. However, it may seem unclear how to deal with an incident electromagnetic field. This suggests to combine them into one matrix equation that can solve for electromagnetic scattering, rather than solving for the electric and magnetic fields separately. Assuming that identical solutions are found for the EFIE and MFIE, the following equation is constructed

$$\begin{bmatrix} \mathbf{D}^1 + \mathbf{D}^2 & -\mathbf{K}^1 - \mathbf{K}^2 \\ \mathbf{K}^1 + \mathbf{K}^2 & \frac{\mathbf{D}^1}{Z_1^2} + \frac{\mathbf{D}^2}{Z_2^2} \end{bmatrix} \boldsymbol{\psi} = \mathbf{q}. \quad (3.36)$$

All that has been done is to put the EFIE in the top half of the matrix and the MFIE in the bottom half. This is done so simply since the EFIE and MFIE have the same solution. The initial conditions have the following form

$$\mathbf{q} = \begin{cases} \int_{S_m} dS \mathbf{f}_m(\mathbf{r}) \cdot \mathbf{E}_1^{inc}(\mathbf{r}) : & m = 1 \dots N \\ \int_{S_{m-N}} dS \mathbf{f}_{m-N}(\mathbf{r}) \cdot \mathbf{H}_1^{inc}(\mathbf{r}) : & m = N + 1 \dots 2N \end{cases}. \quad (3.37)$$

No more manipulation of the surface integral equations is needed [2]. Assuming the Green's functions can be found, one can numerically integrate the surface integrals needed to calculate each matrix element and the initial condition vector \mathbf{q} . Chapter

4 is dedicated to describing how such integrals are calculated. Eq. (3.36) can be solved by inverting the matrix. Chapter 5 presents the Robin Hood method, which is the algorithm used to solve Eq. (3.36). Once α and β are found, the electric and magnetic fields can be generated from the surface current densities. Performing similar manipulations that gave (3.18), one obtains the electric field

$$\mathbf{E}_i(\mathbf{r}) = \begin{cases} + \\ - \end{cases} \sum_{n=1}^N \left(-\alpha_n \frac{\omega\mu_i}{i} \int_{S_n} dS' \bar{\mathbf{G}}_i(\mathbf{r}, \mathbf{r}') \cdot \mathbf{f}_n(\mathbf{r}') - \beta_n \int_{S_n} dS' [\nabla' \times \bar{\mathbf{G}}_i(\mathbf{r}, \mathbf{r}')] \cdot \mathbf{f}_n(\mathbf{r}') \right) + \begin{cases} \int_{S_m} dS \mathbf{f}_m(\mathbf{r}) \cdot \mathbf{E}_1^{inc}(\mathbf{r}) : & i = 1 \text{ and } \mathbf{r} \in V_1 \\ 0 : & i = 2 \text{ and } \mathbf{r} \in V_2 \end{cases} \quad (3.38)$$

The magnetic field is given by

$$\mathbf{H}_i(\mathbf{r}) = \begin{cases} + \\ - \end{cases} \sum_{n=1}^N \left(-\beta_n \frac{\omega\epsilon_i}{i} \int_{S_n} dS' \bar{\mathbf{G}}_i(\mathbf{r}, \mathbf{r}') \cdot \mathbf{f}_n(\mathbf{r}') + \alpha_n \int_{S_n} dS' [\nabla' \times \bar{\mathbf{G}}_i(\mathbf{r}, \mathbf{r}')] \cdot \mathbf{f}_n(\mathbf{r}') \right) + \begin{cases} \int_{S_m} dS \mathbf{f}_m(\mathbf{r}) \cdot \mathbf{H}_1^{inc}(\mathbf{r}) : & i = 1 \text{ and } \mathbf{r} \in V_1 \\ 0 : & i = 2 \text{ and } \mathbf{r} \in V_2 \end{cases} \quad (3.39)$$

Now that the surface integral equations have been derived in matrix form and all of the equations have been presented, the next chapter will describe the techniques used to evaluate the Green's functions and surface integrals.

Chapter 4

Evaluating Dyadic Green's Functions and Surface Integrals

Recall from Eq. (3.11) that the Dyadic Green's function is the following

$$\bar{\mathbf{G}}_i(\mathbf{r}, \mathbf{r}') = \left(\bar{\mathbf{I}} + \frac{\nabla\nabla}{k_i^2} \right) \frac{e^{ik_i R}}{4\pi R} = \left(\bar{\mathbf{I}} + \frac{\nabla\nabla}{k_i^2} \right) G_i(\mathbf{r}, \mathbf{r}'). \quad (4.1)$$

It is clear to see that as $\mathbf{r} \rightarrow \mathbf{r}'$, or as $R \rightarrow 0$, the scalar Green's function is singular. Furthermore, the two gradients acting on it make it become even more singular. For overlapping triangles, numerical integration would not give accurate results for the matrix elements because of the singularities. A clever trick known as the singularity subtraction method can be used to work around this dilemma. Hanninen, Taskinen, and Sarvas [3] present this method, which will be described below.

4.1 Singularity Subtraction of Green's functions

The singularity subtraction method separates the scalar Green's function into a singular and smooth part. Taylor expanding the scalar Green's function allows for the singular portion to be removed, which leaves the smooth Green's function to be numerically integrated. The singular part of the Green's function must be integrated by a closed form and then added back later to recover the full scalar Green's function.

Taylor expanding gives

$$G_i(\mathbf{r}, \mathbf{r}') = \frac{1}{4\pi} \sum_{q=-1}^{\infty} \frac{(ik_i)^{q+1} R^q}{(q+1)!} = \frac{1}{4\pi} \left(\frac{1}{R} + ik_i - \frac{k_i^2 R}{2} + \frac{ik_i^3 R^2}{6} - \dots \right). \quad (4.2)$$

The first two odd terms are the singular part. One might think only the $1/R$ term needs to be removed, but the derivative of the Green's function is discontinuous at $R = 0$. In principle, all of the odd terms would need to be removed. However, the singularity only occurs as $k_i R \rightarrow 0$, so higher order odd terms would be negligible. For this reason, only the two first odd terms are removed. If greater accuracy is needed, more terms can be removed [23]. Subtracting the first two odd terms gives the smooth Green's function

$$G_i^s(\mathbf{r}, \mathbf{r}') = \frac{1}{4\pi} \left(\frac{e^{ik_i R} - 1}{R} + \frac{k_i^2 R}{2} \right). \quad (4.3)$$

Now, this part of the Green's function can be solved using numerical integration.

Next, the two integrals needed for the matrix elements D_{mn}^i and K_{mn}^i will be simplified in terms of the scalar Green's function. This will illustrate which integrals are needed to determine the singular part of the Green's function. D_{mn}^i has the following integral

$$\begin{aligned} & \int_{S_m} dS \mathbf{f}_m(\mathbf{r}) \cdot \left(\frac{\nabla \nabla}{k_i^2} + \bar{\mathbf{1}} \right) \cdot \int_{S_n} dS' G_i(\mathbf{r}, \mathbf{r}') \mathbf{f}_n(\mathbf{r}') \\ &= \frac{1}{k_i^2} \int_{S_m} dS \mathbf{f}_m(\mathbf{r}) \cdot \nabla \int_{S_n} dS' G_i(\mathbf{r}, \mathbf{r}') \nabla' \cdot \mathbf{f}_n(\mathbf{r}') \\ & \quad + \int_{S_m} dS \mathbf{f}_m(\mathbf{r}) \cdot \int_{S_n} dS' G_i(\mathbf{r}, \mathbf{r}') \mathbf{f}_n(\mathbf{r}') \\ &= -\frac{1}{k_i^2} \int_{S_m} dS [\nabla \cdot \mathbf{f}_m(\mathbf{r})] \int_{S_n} dS' G_i(\mathbf{r}, \mathbf{r}') \nabla' \cdot \mathbf{f}_n(\mathbf{r}') \\ & \quad + \int_{S_m} dS \mathbf{f}_m(\mathbf{r}) \cdot \int_{S_n} dS' G_i(\mathbf{r}, \mathbf{r}') \mathbf{f}_n(\mathbf{r}') \end{aligned} \quad (4.4)$$

The first step moves the ∇ -operator into the integral and changes it to ∇' by integration by parts and applying Gauss' theorem. The same is done in the second step to move the ∇ -operator to act on \mathbf{f}_m .

Similarly, K_{mn}^i can be manipulated by applying the following identity, Eq. (8.2.16b) in [24],

$$\nabla' \times \bar{\mathbf{G}}_i(\mathbf{r}, \mathbf{r}') = [\nabla' G_i(\mathbf{r}, \mathbf{r}')] \times \bar{\mathbf{1}} = -[\nabla G_i(\mathbf{r}, \mathbf{r}')] \times \bar{\mathbf{1}}, \quad (4.5)$$

which allows K_{mn}^i to become

$$\begin{aligned} & \int_{S_m} dS \mathbf{f}_m(\mathbf{r}) \cdot \int_{S_n} dS' [\nabla' \times \bar{\mathbf{G}}_i(\mathbf{r}, \mathbf{r}')] \cdot \mathbf{f}_n(\mathbf{r}') \\ &= \int_{S_m} dS \mathbf{f}_m(\mathbf{r}) \cdot \int_{S_n} dS' [\nabla' G_i(\mathbf{r}, \mathbf{r}')] \times \mathbf{f}_n(\mathbf{r}'). \end{aligned} \quad (4.6)$$

By looking at Eqs. (4.4) and (4.6), note that three types of integrals are needed. Taylor expanding G_i in terms of kR , the following three integrals are needed to evaluate the singular part of the Green's function

$$K_1^q(\mathbf{f}_n) = \int_{S_n} dS' R^q \nabla' \cdot \mathbf{f}_n(\mathbf{r}'), \quad (4.7)$$

$$\mathbf{K}_2^q(\mathbf{f}_n) = \int_{S_n} dS' R^q \mathbf{f}_n(\mathbf{r}'), \quad (4.8)$$

$$\mathbf{K}_4^q(\mathbf{f}_n) = \int_{S_n} dS' (\nabla' R^q) \times \mathbf{f}_n(\mathbf{r}'). \quad (4.9)$$

The integrals are labelled this way to agree with Hanninen, Taskinen, and Sarvas [3]. Note that these integrals must be calculated for $q = -1$ and 1 , or as many odd terms are desired. The following integral will be calculated as well as an intermediate to help compute Eq. (4.9)

$$\mathbf{K}_3^q(\mathbf{f}_n) = \int_{S_n} dS' \nabla' R^q. \quad (4.10)$$

After these are found, the outer integrals in Eqs. (4.4) and (4.6) easily. Since very small triangles are assumed, the outer integrand is evaluated at the center of the triangle and integration is avoided completely.

4.2 Calculating the Singular Part of Green's Functions

The integrals (4.7), (4.8), and (4.9) can be evaluated in closed form with no approximations. To do so, they will be reduced to the following line and surface integrals

$$I_q^L(\Delta L) = \int_{\Delta L} R^q dl', \quad (4.11)$$

$$I_q^S(S) = \int_S R^q dS', \quad (4.12)$$

which can be recursively generated. Using Eq. (3.25) allows for K_1^q to be expressed as a constant times a surface integral

$$K_1^q(T^\pm) = \int_{S_n} dS' R^q \nabla' \cdot \mathbf{f}_n(\mathbf{r}') = \pm \frac{L}{A^\pm} \int_{T^\pm} dS' R^q = \pm \frac{L}{A^\pm} I_q^S(T^\pm). \quad (4.13)$$

To simplify \mathbf{K}_2^q , the quantity $\boldsymbol{\rho}$ is introduced,

$$\boldsymbol{\rho} = \mathbf{r} - \hat{\mathbf{n}}(\mathbf{r}')(\hat{\mathbf{n}}(\mathbf{r}') \cdot (\mathbf{r} - \mathbf{r}')), \quad (4.14)$$

which has the following property involving a surface gradient

$$\nabla'_s R^{q+2} = (q+2)(\mathbf{r}' - \boldsymbol{\rho})R^q. \quad (4.15)$$

Using Gauss' theorem will allow this manipulation

$$\int_{T^\pm} dS' \nabla'_s R^q = \int_{\partial T^\pm} dl' \hat{\mathbf{m}}(\mathbf{r}) R^q, \quad (4.16)$$

where $\hat{\mathbf{m}}$ is the unit vector pointing out of each side of the triangle and ∂T^\pm refers to the side of each triangle. Using Eqs. (4.14), (4.15), and (4.16), \mathbf{K}_2^q can be simplified

to become the following

$$\begin{aligned}
\mathbf{K}_2^q(T^\pm) &= \int_{T^\pm} dS' R^q \mathbf{f}_n(\mathbf{r}') = \pm \frac{L}{2A^\pm} \int_{T^\pm} dS' R^q [(\mathbf{r}' - \boldsymbol{\rho}) + (\boldsymbol{\rho} - \mathbf{p}^\pm)] \\
&= \pm \frac{L}{2A^\pm} \left(\frac{1}{q+2} \int_{T^\pm} dS' \nabla'_s R^{q+2} + (\boldsymbol{\rho} - \mathbf{p}^\pm) \int_{T^\pm} dS' R^q \right) \\
&= \pm \frac{L}{2A^\pm} \left(\frac{1}{q+2} \sum_{i=1}^3 \hat{\mathbf{m}}_i \int_{\partial T_i^\pm} dl' R^{q+2} + (\boldsymbol{\rho} - \mathbf{p}^\pm) \int_{T^\pm} dS' R^q \right) \\
&= \pm \frac{L}{2A^\pm} \left(\frac{1}{q+2} \sum_{i=1}^3 \hat{\mathbf{m}}_i I_{q+2}^L(\partial T_i^\pm) + (\boldsymbol{\rho} - \mathbf{p}^\pm) I_q^S(T^\pm) \right). \quad (4.17)
\end{aligned}$$

To compute \mathbf{K}_4^q , the integral \mathbf{K}_4^q will first be found. If the gradient is broken up into surface and normal components, then

$$\mathbf{K}_3^q(T^\pm) = \int_{T^\pm} dS' \nabla' R^q = \int_{T^\pm} dS' \nabla'_s R^q + \int_{T^\pm} dS' \nabla'_n R^q. \quad (4.18)$$

Eqs. (4.15) and (4.16) show how to reduce the surface gradient term into a line integral. The normal gradient is simplified by the following

$$\nabla'_n R^q = \hat{\mathbf{n}}(\mathbf{r}') (\hat{\mathbf{n}}(\mathbf{r}') \cdot \nabla') R^q = -\hat{\mathbf{n}}(\mathbf{r}') (\hat{\mathbf{n}}(\mathbf{r}') \cdot (\mathbf{r} - \mathbf{r}')) q R^{q-2} = -\hat{\mathbf{n}}(\mathbf{r}') h q R^{q-2}, \quad (4.19)$$

where h is defined as $\hat{\mathbf{n}}(\mathbf{r}') \cdot (\mathbf{r} - \mathbf{r}')$. Putting these surface and normal gradient definitions together solves for \mathbf{K}_3^q in terms of line and surface integrals

$$\mathbf{K}_3^q(T^\pm) = \sum_{i=1}^3 \hat{\mathbf{m}}_i I_q^L(\partial T_i^\pm) - h q \hat{\mathbf{n}} I_{q-2}^S(T^\pm). \quad (4.20)$$

Next, \mathbf{K}_4^q will be simplified in terms of a cross product with \mathbf{K}_3^q as follows

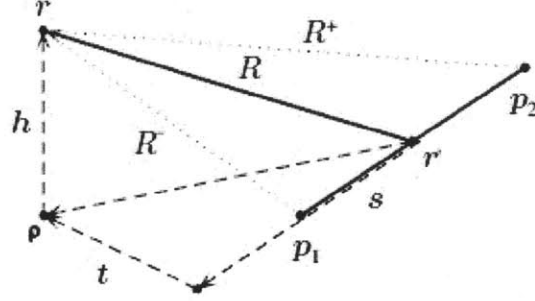
$$\begin{aligned}
\mathbf{K}_4^q(T^\pm) &= \int_{S_n} dS' (\nabla' R^q) \times \mathbf{f}_n(\mathbf{r}') = \pm \frac{L}{2A^\pm} \int_{T^\pm} dS' \nabla' R^q \times (\mathbf{r}' - \mathbf{p}^\pm) \\
&= \pm \frac{L}{2A^\pm} \int_{T^\pm} dS' \nabla' R^q \times ((\mathbf{r}' - \mathbf{r}) + (\mathbf{r} - \mathbf{p}^\pm)) \\
&= \pm \frac{L}{2A^\pm} \int_{T^\pm} dS' \nabla' R^q \times (\mathbf{r}' - \mathbf{r}) \mp \frac{L}{2A^\pm} (\mathbf{r} - \mathbf{p}^\pm) \times \int_{T^\pm} dS' \nabla' R^q \\
&= \mp \frac{L}{2A^\pm} (\mathbf{r} - \mathbf{p}^\pm) \times \int_{T^\pm} dS' \nabla' R^q = \mp \frac{L}{2A^\pm} (\mathbf{r} - \mathbf{p}^\pm) \times \mathbf{K}_3^q(T^\pm), \quad (4.21)
\end{aligned}$$

where $\nabla' R^q \times (\mathbf{r}' - \mathbf{r}) = 0$ was used to obtain the final expression.

4.2.1 Calculation of Line and Surface Integrals

Now, all of the needed integrals to calculate the singular Green's functions are expressed in terms of line and surface integrals. To evaluate these integrals, a few quantities must be introduced. \mathbf{p}_1 and \mathbf{p}_2 are the end points of the common edge with a length of ΔL . \mathbf{r}' is located on the line segment ΔL , which moves across the whole segment as the integration variable. \mathbf{r} is located on a completely different triangle, which allows a correlation between all of the edges to be found. Typically, one would integrate over every point \mathbf{r} on the triangle and \mathbf{r}' along the edge. However, since the triangles are small, the center of the triangle and edge is used to evaluate the integrands and integration can be completely avoided. A new cartesian coordinate system is introduced with respect to the line segment as $\mathbf{r} - \mathbf{r}' = \mathbf{s} + \mathbf{t} + \mathbf{h}$, as shown in Fig. 4-1. $\hat{\mathbf{s}} = (\mathbf{p}_2 - \mathbf{p}_1)/|\mathbf{p}_2 - \mathbf{p}_1|$ and points along the direction of the line. $\hat{\mathbf{t}}$ is perpendicular to $\hat{\mathbf{s}}$ and is in the plane of the triangle. $\hat{\mathbf{h}}$ is perpendicular to both of these, and therefore points out of the plane of the triangle towards \mathbf{r} .

Figure 4-1: The coordinate system with three orthogonal vectors: $\hat{\mathbf{h}}$, $\hat{\mathbf{s}}$, and $\hat{\mathbf{t}}$. \mathbf{r}' represents a point along the edge of the two triangles and \mathbf{r} is on the triangles of the other edge [3].



The following are needed to compute I_{-1}^L

$$R_0^2 = t^2 + h^2 = R^2 - s^2 \quad (4.22)$$

$$s^+ = (\mathbf{p}_2 - \mathbf{r}) \cdot \hat{\mathbf{s}} \quad (4.23)$$

$$s^- = (\mathbf{p}_1 - \mathbf{r}) \cdot \hat{\mathbf{s}} \quad (4.24)$$

$$R^+ = \sqrt{(s^+)^2 + R_0^2} = |\mathbf{r} - \mathbf{p}_2| \quad (4.25)$$

$$R^- = \sqrt{(s^-)^2 + R_0^2} = |\mathbf{r} - \mathbf{p}_1|. \quad (4.26)$$

To find I_{-1}^L , it is reexpressed as

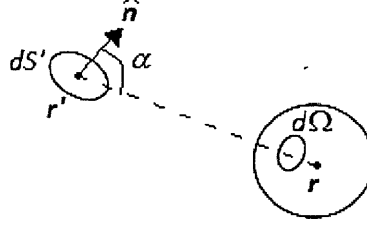
$$I_{-1}^L(\Delta L) = \int_{\Delta L} \frac{1}{R} dl' = \int_{s^-}^{s^+} \frac{1}{\sqrt{s^2 + R_0^2}} ds, \quad (4.27)$$

where $R_0^2 > 0$. In other words, \mathbf{r} cannot be on the line L . Fortunately, if this does occur, this integral will be cancelled out and not affect the matrix elements.

Performing the integral gives

$$I_{-1}^L(\Delta L) = \int_{s^-}^{s^+} \frac{1}{\sqrt{s^2 + R_0^2}} ds = \ln \left(s^+ + \sqrt{(s^+)^2 + R_0^2} \right) - \ln \left(s^- + \sqrt{(s^-)^2 + R_0^2} \right). \quad (4.28)$$

Figure 4-2: The solid angle $d\Omega$ depends on the angle α , the normal vector $\hat{\mathbf{n}}$, and the vector $\mathbf{r} - \mathbf{r}'$.



Substituting in R^+ and R^- gives

$$I_{-1}^L(\Delta L) = \ln \left(\frac{R^+ + s^+}{R^- + s^-} \right) = \ln \left(\frac{R^- - s^-}{R^+ - s^+} \right). \quad (4.29)$$

Note that the denominator of either expression with the largest absolute value should be used for the best numerical accuracy. To calculate all other odd ordered line integrals, an upward recursion relationship will be derived later.

The lowest order surface integral needed is I_{-3}^S . Consider some flat surface S' which will be integrated over with $\hat{\mathbf{n}}$ being the unit vector pointing out of the surface. This integral is computed by considering the solid angle Ω of S' seen from \mathbf{r} . The angle α is introduced, which is defined as $\cos(\alpha) = h/R$. Fig. 4-2 shows this scenario. This allows the following manipulations

$$\Omega = \int_{S'} d\Omega = \int_{S'} \frac{\cos(\alpha)}{R^2} dS' = \int_{S'} \frac{h}{R^3} dS', \quad (4.30)$$

$$I_{-3}^S(S') = \int_{S'} dS' \frac{1}{R^3} = \frac{1}{h} \Omega. \quad (4.31)$$

Fortunately, $h = 0$ never causes a singularity because whenever I_{-3}^S is needed, another factor of h appears in the numerator to cancel the denominator. To solve for the solid angle of triangles, the Euler-Eriksson's formula is used [25]

$$|\Omega| = 2 \arctan(y/x), \quad (4.32)$$

where the phase must be chosen as $-\pi \leq \arctan(y/x) \leq \pi$ for $x, y \in \mathbb{R}$. Furthermore,

$$x = 1 + \mathbf{a}_1 \cdot \mathbf{a}_2 + \mathbf{a}_1 \cdot \mathbf{a}_3 + \mathbf{a}_2 \cdot \mathbf{a}_3, \quad y = |\mathbf{a}_1 \cdot (\mathbf{a}_2 \times \mathbf{a}_3)|, \quad (4.33)$$

$$\mathbf{a}_n = \frac{\mathbf{p}_n - \mathbf{r}}{|\mathbf{p}_n - \mathbf{r}|}, \quad n = 1, 2, 3, \quad (4.34)$$

where $\mathbf{p}_1, \mathbf{p}_2$, and \mathbf{p}_3 are the three vertices of the triangle. They are labelled in positive rotation with respect to $\hat{\mathbf{n}}$, which is defined as the following

$$\hat{\mathbf{n}} = \frac{(\mathbf{p}_2 - \mathbf{p}_1) \times (\mathbf{p}_3 - \mathbf{p}_1)}{|(\mathbf{p}_2 - \mathbf{p}_1) \times (\mathbf{p}_3 - \mathbf{p}_1)|}. \quad (4.35)$$

The other surface integrals will also be calculated in terms of a recursive formula, which will be derived next.

The only integrals that are needed are of odd order q with $q \geq -1$ for the line integrals and $q \geq -3$ for the surface integrals. An upward recursion formula can be found that can find all of the odd terms from the integrals previously calculated in closed form. To start, note that

$$R^q = R^{q-2}R^2 = R^{q-2}(s^2 + r_0^2), \quad (4.36)$$

which allows I_q^L to be written as

$$I_q^L(\Delta L) = \int_{\Delta L} dl' R^q = R_0^2 \int_{\Delta L} dl' R^{q-2} + \int_{\Delta L} dl' s^2 R^{q-2}. \quad (4.37)$$

The second term can be manipulated by using the following relationship

$$\frac{\partial}{\partial s} R^q = qsR^{q-2}, \quad (4.38)$$

which allows integration by parts to be used to simplify the second term

$$\int_{\Delta L} dl' s^2 R^{q-2} = \frac{1}{q} [sR^q]_{s=s^-}^{s=s^+} - \frac{1}{q} \int_{\Delta L} dl' R^q = \frac{1}{q} [sR^q]_{s=s^-}^{s=s^+} - \frac{1}{q} I_q^L. \quad (4.39)$$

From here, I_q^L can be solved, which gives the recursion relationship

$$I_q^L(\Delta L) = \frac{qR_0^2}{q+1} I_{q-2}^L(\Delta L) + \frac{1}{q+1} (s^+(R^+)^q - s^-(R^-)^q). \quad (4.40)$$

Now, the surface integral formula must be derived. To do so, a fairly complicated manipulation must be done. Starting with the surface divergence,

$$\begin{aligned} \nabla'_s \cdot ((\mathbf{r} - \mathbf{r}')R^q) &= (\nabla'_s \cdot (\mathbf{r} - \mathbf{r}'))R^q + (\mathbf{r} - \mathbf{r}')(\nabla'_s \cdot R^q) \\ &= -2R^q + q(\mathbf{r} - \mathbf{r}') \cdot (\mathbf{r}' - \boldsymbol{\rho})R^{q-2} \\ &= -2R^q + q(\mathbf{r} - \mathbf{r}') \cdot ((\mathbf{r}' - \mathbf{r}) + (\mathbf{r} - \boldsymbol{\rho}))R^{q-2} \\ &= -2R^q - qR^q + q(\mathbf{r} - \mathbf{r}') \cdot (\mathbf{r} - \boldsymbol{\rho})R^{q-2} \\ &= -2R^q - qR^q + qh^2R^{q-2} \end{aligned} \quad (4.41)$$

Putting R^q on one side by itself and taking the appropriate surface integral gives

$$I_q^S(S) = \int_S dS' R^q = \frac{qh^2}{q+2} \int_S dS' R^{q-2} - \frac{1}{q+2} \int_S \nabla'_s \cdot ((\mathbf{r} - \mathbf{r}')R^q) dS'. \quad (4.42)$$

Applying Gauss' theorem to the last term allows it to be expressed as a line integral, which was shown previously in Eq. (4.16). This gives

$$I_q^S(S) = \frac{qh^2}{q+2} I_{q-2}^S(s) - \frac{1}{q+2} \sum_{i=1}^3 \hat{\mathbf{m}}_i \cdot (\mathbf{r} - \mathbf{r}') I_q^L(\partial S_i). \quad (4.43)$$

The recursive formulae, Eqs. (4.40) and (4.43), in combination with Eqs. (4.29) and (4.31) allow for the singular Green's function integrals to be calculated. Once this is done, the smooth Green's function integrals can be taken using any numerical integrator and added to singular part to obtain a well behaved Green's function. Once this is done, all of the matrix elements giving the correlation between each triangle edge can be calculated. From here, all that is needed to solve for electromagnetic scattering is to use an algorithm to solve the matrix equation.

Chapter 5

Using the Robin Hood Method to Solve Matrix Equations

In principle, once all of the matrix elements and the vector containing the incident fields is computed, the solution should be simple to find. Inverting the matrix and multiplying by the vector will give the desired solution. However, the matrix is particularly large, which causes issues with memory allocation. These computational constraints make it difficult to solve problems with geometries broken into more than 10,000 elements, since memory scales quadratically with the number of elements. To analyze KATRIN's spectrometer, it must be broken up into about that many elements. For this reason, the matrix must be inverted in a clever way that never stores the whole matrix in memory.

The Robin Hood method (RH) is a matrix inversion algorithm, which was initially used to solve electrostatic problems. Recently, it has been expanded to solve dielectric and magnetic materials problems. It is well suited for solving problems with well-defined boundary conditions. It is particularly successful because it decreases the memory footprint to scale as N , rather than N^2 for typical approaches. RH can be applied only to matrices that are diagonally dominant. Fortunately, most Green's functions guarantee this. The system also must be linear, which is implied by Maxwell's equations. Furthermore, the solution must be unique.

5.1 Robin Hood Derivation for Electrostatic Problems

The fundamental steps of RH are most clearly seen when solving electrostatic problems. It has simple boundary conditions, which allows the derivation to focus on the details of RH, rather than other complications. Consider some metal conductor with arbitrary shape. The goal is to calculate the charge distribution, given the constraints on the potential ϕ . Gauss's law, $\nabla \cdot \mathbf{E} = \rho/\epsilon_0$, and applying $\mathbf{E} = \nabla\phi$ gives Poisson's electrostatic equation

$$\nabla^2\phi = -\frac{\rho}{\epsilon_0}. \quad (5.1)$$

A Green's function is needed to generate the potential from the charges. Since the surface is discretized, it makes sense to work with charge densities, which can be specified on each element. To find the potential, the following Green's function is introduced

$$\phi(\mathbf{r}) = \int_{\partial V} dS' G_P(\mathbf{r}, \mathbf{r}') \sigma(\mathbf{r}'), \quad (5.2)$$

where σ is the charge density, and a subscript P for Poisson is placed on the Green's function to not confuse it with the scalar Green's function introduced in chapter 3. This particular Green's function can be shown to have the following form

$$G_P(\mathbf{r}, \mathbf{r}') = \frac{1}{4\pi\epsilon_0} \frac{1}{|\mathbf{r} - \mathbf{r}'|}. \quad (5.3)$$

Assuming infinitesimal discretization states that the charge density is constant over each element. This allows the integral equation (5.2) to be expressed as a matrix equation

$$\phi_i = \sum_{j=0}^N I_{ij} \sigma_j, \quad (5.4)$$

where ϕ_i refers to the potential on the element i , σ_j refers to the charge density on

element j , N is the total number of elements, and the matrix element I_{ij} is

$$I_{ij} = \frac{1}{4\pi\epsilon_0} \int_{\Delta S_j} \frac{dS_j}{|\mathbf{r}_i - \mathbf{r}_j|}, \quad (5.5)$$

where \mathbf{r}_i refers to the center of the element i . The only other information needed to apply RH is the boundary conditions. For a metal conductor, the potential at the surface should be equal everywhere, which are the necessary boundary conditions. This constrains the set of potentials ϕ_i . Since RH is designed to solve this equation, it can be classified as a boundary element method (BEM).

Conceptually, RH does the following. A total charge Q is assumed to be spread throughout the surface. An initial random charge distribution is assigned to each element, which is expected to be incorrect. Next, the potential on each element is calculated due to these incorrect charge distributions. This potential is compared to the known potential distribution. The two elements with a potential furthest away from the average potential are labelled as elements m and n . The charge is then changed between the two elements to put them at the same potential. This process is repeated iteratively until the potential is equal on every element within some specified accuracy.

The change in charge density can be found from charge conservation

$$\delta q_{tot} = 0 = \delta\sigma_m A_m + \delta\sigma_n A_n \quad (5.6)$$

$$\delta\sigma_m = \frac{A_n(\phi_n - \phi_m)}{A_n(I_{mm} - I_{nm}) + A_m(I_{nn} - I_{mn})}, \quad (5.7)$$

$$\delta\sigma_n = \frac{A_m(\phi_m - \phi_n)}{A_n(I_{mm} - I_{nm}) + A_m(I_{nn} - I_{mn})}, \quad (5.8)$$

since charge conservation requires the same amount of charge to be transferred between elements and where A_i is the area of element i . The new potentials ϕ'_m and ϕ'_n can then be found by the following equations

$$\phi'_m = \phi_m + I_{mm}\delta\sigma_m + I_{mn}\delta\sigma_n, \quad (5.9)$$

$$\phi'_n = \phi_n + I_{nn}\delta\sigma_n + I_{nm}\delta\sigma_m. \quad (5.10)$$

Now the two potentials ϕ'_m and ϕ'_n are at the same value. Furthermore, the change in charge propagates to adjacent elements, which ensures quick convergence.

A slightly different example of using RH is to solve for the charge density of each element given a constant potential ϕ_0 which is supplied by an external source. In this case, charge is not conserved and different amounts of charge can be distributed between the two elements with a potential furthest away from ϕ_0 . The potentials ϕ_m and ϕ_n are then set to be equal to ϕ_0 by distributing charges as follows [?]

$$\delta\sigma_m = \frac{(\phi_0 - \phi_m)I_{nn} - (\phi_0 - \phi_n)I_{mn}}{I_{mm}I_{nn} - I_{mn}I_{nm}}, \quad (5.11)$$

$$\delta\sigma_n = \frac{(\phi_0 - \phi_n)I_{mm} - (\phi_0 - \phi_m)I_{nm}}{I_{mm}I_{nn} - I_{mn}I_{nm}}. \quad (5.12)$$

The beauty in RH lies in the fact that it is very simple conceptually, yet still can achieve accurate results with low memory costs. The algorithm's performance has been well tested. The number of iterations increases logarithmically with the desired accuracy. The number of iterations increases linearly and the convergence time increases quadratically with the number of elements. The algorithm lends itself to be used with parallel processors very effectively. Currently, RH has computed the most accurate calculation on the capacitance for a cube [26].

5.2 Robin Hood Applied to Electromagnetic Scattering Problems

Now that RH has been shown on the simplest example, it now can be used for solving electromagnetic scattering problems. The previous RH formulation must be slightly altered because the matrix equation contains complex quantities, rather than real quantities. The complex quantities come from the electric field wave equation, Eq. (3.6), and the Green's functions, Eq. (3.11). Furthermore, since there are electric and magnetic coefficients, α_i and β_i , RH cannot allow the electric and magnetic current densities to get switched between each other. In other words, only the α_i 's should

be switching with each other, and only the β_i 's should be moved between each other.
Note that RH has never been used to solve complex matrix equations previously.

Chapter 6

Scattering by Spheres: Comparing RH and Mie Scattering

Before applying RH with the derived surface integral equations to KATRIN's spectrometer, it should be tested against a simpler system with an analytic solution. The sphere is the simplest example of a 3D scatterer and is essentially the only one with an analytic solution, which is known as Mie scattering, or the Mie solution. For this reason, the Mie solution must be studied to compare to the MoM formulation.

6.1 Implementation of Mie Scattering

Mie scattering is an exact solution of Maxwell's equations, which was found in 1908. It gives various quantities for electromagnetic radiation scattering off of a spherically symmetric particle. Mie scattering is the generalization of Rayleigh scattering, which only applies for very small particles. This section describes the main results of the analytic solution and shows how it was implemented to get accurate solutions. Once the code for Mie scattering is confirmed, it can be used to compare to RH. Once these two agree, the surface integral equations can be applied to more complex geometries.

6.1.1 Mie Scattering Equations

Texts such as Kerker [27] and Bohren and Huffman [28] marvelously explain the derivation of Mie scattering, so only the relevant results will be presented. When one solves Maxwell's equations with the proper boundary conditions, the electric and magnetic fields can be found for the incident and scattered regimes. These can be compared to find the differential scattering cross section $\frac{d\sigma}{d\Omega}$.

Since the particle is a sphere, spherical coordinates are used, and the solutions to Maxwell's equations are broken up into a radial and angular component. The radial solution gives Ricatti-Bessel functions ($\psi_n(z)$, $\chi_n(z)$, $\xi_n(z)$, and $\zeta_n(z)$). They have the following identities

$$\psi_n(z) = (\pi z/2)^{1/2} J_{n+\frac{1}{2}}(z) = z j_n(z) \quad (6.1)$$

$$\chi_n(z) = -(\pi z/2)^{1/2} Y_{n+\frac{1}{2}}(z) = -z y_n(z) \quad (6.2)$$

$$\xi_n(z) = \psi_n(z) - i\chi_n(z) = z h_n^{(1)}(z) \quad (6.3)$$

$$\zeta_n(z) = \psi_n(z) + i\chi_n(z) = z h_n^{(2)}(z), \quad (6.4)$$

where $J_n(z)$ and $Y_n(z)$ are the Bessel function of the first and second kind, $j_n(z)$ and $y_n(z)$ are the spherical Bessel functions of first and second kind, and $h_n^{(1)}(z)$ and $h_n^{(2)}(z)$ are the spherical Hankel function of the first and second kind.

Solving for the angular part of Maxwell's equations leads to the necessity of Legendre polynomials: $P_n^{(1)}(x)$. Two coefficients (π_n and τ_n) involving Legendre polynomials are assigned for convenience

$$\pi_n(\cos \theta) = \frac{P_n^{(1)}(\cos \theta)}{\sin \theta} \quad (6.5)$$

$$\tau_n(\cos \theta) = \frac{d}{d\theta} P_n^{(1)}(\cos \theta) \quad (6.6)$$

When considering the total solution for the scattered part, which are broken into

two polarization components, two more coefficients (a_n and b_n) are convenient

$$a_n = \frac{\psi_n(x)\psi'_n(mx) - m\psi_n(mx)\psi'_n(x)}{\xi_n(x)\psi'_n(mx) - m\psi_n(mx)\xi'_n(x)} \quad (6.7)$$

$$b_n = \frac{m\psi_n(x)\psi'_n(mx) - \psi_n(mx)\psi'_n(x)}{m\xi_n(x)\psi'_n(mx) - \psi_n(mx)\xi'_n(x)}, \quad (6.8)$$

where m is the complex refractive index of the spherical object, $x = 2\pi a/\lambda$, a is the radius of the particle, and λ is the wavelength of the incident light. These equations are in the form given by Bohren and Huffman. Interestingly enough, Kerker has ζ 's instead of ξ 's, but the difference produces the same results.

Assuming that the incident wave travels in the z direction and the electric field is in the x direction, the scattered electric field can be represented in terms of a ϕ component and a θ component. In the far field limit, the $(1/r^2)$ term dies off, and there are spherical waves falling off as $(1/r)$. In other words,

$$E_\phi = -\frac{ie^{-kr}}{kr}S_1 \sin \phi \quad (6.9)$$

$$E_\theta = \frac{ie^{-kr}}{kr}S_2 \cos \phi, \quad (6.10)$$

where S_1 and S_2 are amplitude functions defined as the following

$$S_1 = \sum_{n=1}^{\infty} \frac{2n+1}{n(n+1)} (a_n \pi_n(\cos \theta) + b_n \tau_n(\cos \theta)) \quad (6.11)$$

$$S_2 = \sum_{n=1}^{\infty} \frac{2n+1}{n(n+1)} (a_n \tau_n(\cos \theta) + b_n \pi_n(\cos \theta)) \quad (6.12)$$

From here, multiple quantities can be calculated. Q_{sca} is a scattering efficiency, which is given by the following equation:

$$Q_{sca} = \sum_{n=1}^{\infty} \frac{2}{x^2} (2n+1) (|a_n|^2 + |b_n|^2) \quad (6.13)$$

This quantity is useful for comparison because multiple papers calculate it extensively.

Furthermore, the Mie solution gives scattering cross sections, which are broken

into two polarizations

$$\frac{d\sigma_\phi}{d\Omega} = \frac{\lambda^2}{4\pi^2} |S_1|^2 \quad (6.14)$$

$$\frac{d\sigma_\theta}{d\Omega} = \frac{\lambda^2}{4\pi^2} |S_2|^2 \quad (6.15)$$

Now that all of the quantities needed for Mie scattering calculations are outlined, a discussion will be presented on how to properly implement them.

6.1.2 Implementing and Confirming Mie Scattering

The inputs needed to characterize the problem are the real and imaginary components of m , the particle radius a , the wavelength of the incident light λ , and the point where the fields are to be evaluated. If cross sections are needed, then a scattering angle instead of a point can be supplied. The first quantities that are calculated are the needed Bessel functions. Since ROOT does not allow for Bessel functions with complex arguments, all of them are recursively generated. This can be done using upward or downward recursion relationships. A popular source of code is provided by Wiscombe [29]. Furthermore, Du has extensive analysis on the stability and precision of upward versus downward recursion. Typically upward recursion is quicker, but less stable in certain cases. Du provides an equation which chooses the number of terms needed that allows for upward recursion to be valid, which was employed. It has problems when the imaginary component of mx is large, but this situation will not be encountered [30].

Spherical Bessel functions are what is needed, so the recursion was initiated by

the following

$$j_0(z) = \frac{\sin z}{z} \quad (6.16)$$

$$y_0(z) = -\frac{\cos z}{z} \quad (6.17)$$

$$j_1(z) = \frac{\sin z}{z^2} - \frac{\cos z}{z} \quad (6.18)$$

$$y_1(z) = -\frac{\cos z}{z^2} - \frac{\sin z}{z} \quad (6.19)$$

$$B_n(z) = (2n - 1) \frac{B_{n-1}(z)}{z} - B_{n-2}(z), \quad (6.20)$$

where $B_n(z)$ represents both spherical Bessel functions $j_n(z)$ and $y_n(z)$. Spherical Hankel functions of the first kind ($h_n^{(1)}$) were also calculated from $j_n(z)$ and $y_n(z)$.

Next, the coefficients $\pi_n(\cos\theta)$ and $\tau_n(\cos\theta)$ were created in a manner described by Matzler [31]. Once this was done, the coefficients a_n and b_n could be calculated. They are rewritten in terms of spherical bessel functions below

$$a_n = \frac{j_n(mx)[xj_n(x)]' - j_n(x)[mxj_n(mx)]'}{j_n(mx)[xh_n^{(1)}(x)]' - h_n^{(1)}(x)[mxj_n(mx)]'} \quad (6.21)$$

$$b_n = \frac{j_n(mx)[xj_n(x)]' - j_n(x)[mxj_n(mx)]'}{j_n(mx)[xh_n^{(1)}(x)]' - h_n^{(1)}(x)[mxj_n(mx)]'}, \quad (6.22)$$

where the prime denotes a derivative applied to the statement in brackets with respect to the input of the Bessel function. Matzler gives recursion identities for all of these, which makes them simple to calculate. Once all of this is implemented, the final step was to compare calculated data to known values.

Three different approaches were considered for calculating all of the functions needed. Wiscombe's approach has proved to be reliable and has been a standard approach since 1979, but its implementation is rather complicated. Du provides a more elegant approach which matches Wiscombe's results perfectly. It was simpler because everything is calculated from the generated Bessel functions and the paper also has results for Q_{sca} , S_1 , and S_2 . Matzler's implementation was even more straightforward, but had no comparison with previous calculations. For this reason, Matzler's approach was used and compared with Du's results. Table 6.1 compares the

results obtained with Du's calculations, which all agree (except when the imaginary component of mx is large, as previously mentioned).

6.2 Comparing MoM and RH to the Mie Solution

Now that the Mie scattering simulation is found to agree with previous Mie scattering results, this can be used to test the surface integral formulation against a sphere. The open-source software package VTK was used to model a sphere, which can be found at www.vtk.org. This package allows for a sphere to be created and discretized into triangles. Once this was done, the adjacent triangles must be found and put into pairs. To do this, each triangle is compared and asks if the triangle has two points in common. If this condition is met, then the two triangles are matched together and an edge electrode can be created in KEMField, which is the electromagnetic field simulator used by KATRIN.

Once the elements are created, the matrix containing Green's functions is constructed. Next, the incident fields must be specified. Since this method assumes time-harmonic fields ($\mathbf{F}(\mathbf{r}, t) = \exp(-i\omega t)\mathbf{F}(\mathbf{r})$, where \mathbf{F} represents an electric or magnetic field), a monochromatic plane wave must be specified. Linearly polarized electromagnetic plane waves have the following form [32]

$$\mathbf{E}(\mathbf{r}, t) = E_0 e^{i(\mathbf{k}\cdot\mathbf{r} - \omega t)} \hat{\mathbf{n}}, \quad (6.23)$$

$$\mathbf{B}(\mathbf{r}, t) = \frac{1}{c} E_0 e^{i(\mathbf{k}\cdot\mathbf{r} - \omega t)} (\hat{\mathbf{k}} \times \hat{\mathbf{n}}) = \frac{1}{c} \hat{\mathbf{k}} \times \mathbf{E}, \quad (6.24)$$

where \mathbf{k} has a magnitude of the wavenumber k and points in the direction of the travelling field. $\hat{\mathbf{n}}$ is the polarization vector. Assuming a propagation in the $\hat{\mathbf{z}}$ direction, a wave polarized in the $\hat{\mathbf{x}}$ direction, using $\mathbf{H} = \frac{1}{\mu_0} \mathbf{B}$, and removing the time dependence gives the specified incident fields to be used in the surface integral formulation

Table 6.1: This compares the results for the developed Mie scattering code with the work of Du, who matched the values of Wiscombe identically. Note that it only breaks down when the imaginary component of mx is around 100. Besides those cases, the data agrees with the accepted values within 2 significant digits.

Case	m	x	Q_{sca}	$S_1(0) = S_2(0)$
a (Du)	.75	.099	7.41786×10^{-6}	$1.81756 \times 10^{-8} - 1.65423 \times 10^{-4}i$
a (Chester)	.75	.099	7.41786×10^{-6}	$1.81756 \times 10^{-8} - 1.65423 \times 10^{-4}i$
b (Du)	.75	.101	8.03354×10^{-6}	$2.04875 \times 10^{-8} - 1.75642 \times 10^{-4}i$
b (Chester)	.75	.101	8.03354×10^{-6}	$2.04875 \times 10^{-8} - 1.75642 \times 10^{-4}i$
c (Du)	.75	10	2.23226	$55.8066 - 9.75810i$
c (Chester)	.75	10	2.23226	$55.8066 - 9.75810i$
d (Du)	.75	1000	1.99791	$499477 - 13365i$
d (Chester)	.75	1000	2.00367	$499477 - 13365i$
e (Du)	$1.33 - 10^{-5}i$	100	2.09659	$5253.3 - 124.319i$
e (Chester)	$1.33 - 10^{-5}i$	100	2.09659	$5253.3 - 124.319i$
f (Du)	$1.33 - 10^{-5}i$	10000	1.72386	$5.01022 \times 10^7 - 153582i$
f (Chester)	$1.33 - 10^{-5}i$	10000	1.72386	$5.01022 \times 10^7 - 153582i$
g (Du)	$1.5 - i$.055	1.13169×10^{-5}	$7.67526 \times 10^{-5} + 8.34388 \times 10^{-5}i$
g (Chester)	$1.5 - i$.055	1.13169×10^{-5}	$7.67526 \times 10^{-5} + 8.34388 \times 10^{-5}i$
h (Du)	$1.5 - i$.056	1.21631×10^{-5}	$8.10238 \times 10^{-5} + 8.80725 \times 10^{-5}i$
h (Chester)	$1.5 - i$.056	1.21631×10^{-5}	$8.10238 \times 10^{-5} + 8.80725 \times 10^{-5}i$
i (Du)	$1.5 - i$	100	1.28370	$5243.75 - 293.417i$
i (Chester)	$1.5 - i$	100	1.28370	$5243.75 - 293.417i$
j (Du)	$1.5 - i$	10000	1.23657	$5.01092 \times 10^7 - 175340i$
j (Chester)	$1.5 - i$	10000	<i>NaN</i>	<i>NaN</i>
k (Du)	$10 - 10i$	1	2.04941	$0.633248 + 0.417931i$
k (Chester)	$10 - 10i$	1	2.04941	$0.633248 + 0.417931i$
l (Du)	$10 - 10i$	100	1.83679	$5177.81 - 26.3381i$
l (Chester)	$10 - 10i$	100	<i>NaN</i>	<i>NaN</i>
m (Du)	$10 - 10i$	10000	1.79539	$5.01479 \times 10^7 - 120600i$
m (Chester)	$10 - 10i$	10000	<i>NaN</i>	<i>NaN</i>

in region 1

$$\mathbf{E}(\mathbf{r})_1^{inc} = E_0 e^{i(\mathbf{r} \cdot \hat{\mathbf{z}})k} \hat{\mathbf{x}}, \quad (6.25)$$

$$\mathbf{H}(\mathbf{r})_1^{inc} = \frac{1}{\mu_0 c} E_0 e^{i(\mathbf{r} \cdot \hat{\mathbf{z}})k} \hat{\mathbf{y}}. \quad (6.26)$$

Now Eq. (3.37) can be calculated to find \mathbf{q} , which provide the initial conditions for the surface integral formulation. From here, RH can be used to solve for the scattered electric and magnetic fields. Unfortunately, results have not been obtained yet to confirm the Mie solution, which will continue to be pursued over the summer.

Chapter 7

Future Work and Conclusions

7.1 Applying the MoM and RH to the Main Spectrometer

Once the Mie solution is confirmed, KATRIN's main spectrometer is the next geometry to be analyzed. Fortunately, this geometry is already discretized into triangles in KEMField. However, it is not easy to figure out which triangles are adjacent in this framework. For this reason, Prof. Formaggio developed a new basis function, instead of RWG basis functions. These allow for each triangle face to represent an element which is expanded upon, rather than each edge. Before diving into simulation of the main spectrometer, Penning traps will be discussed in more detail.

7.1.1 Simulating Penning Traps

It was discovered that background signals have been introduced due to secondary electrons. Simulations were introduced to study and characterize this background using Kassiopeia, the software package used throughout KATRIN. It provides a wide variety of field calculations. From here, Monte Carlo simulations of measurements can be simulated and compared with experimental data. These simulations were performed to confirm the hypotheses of how and where Penning traps were being created. They also confirmed that background production via photons occurs.

From the start, it was known that MAC-E-Filters caused Penning traps. It was first hypothesized that it was created in the center of the spectrometers. Asymmetric magnetic field measurements proved that the background must come from the ends of the spectrometers. Much careful thought was put into the ground electrodes on the ends of the spectrometers to avoid Penning traps. However, this unexpectedly increased the background rate. From here, it was concluded that the trap must be outside the ground electrode ring. A new electrode was designed with no end ring to exactly adjust to the curvature of the magnetic field lines [4].

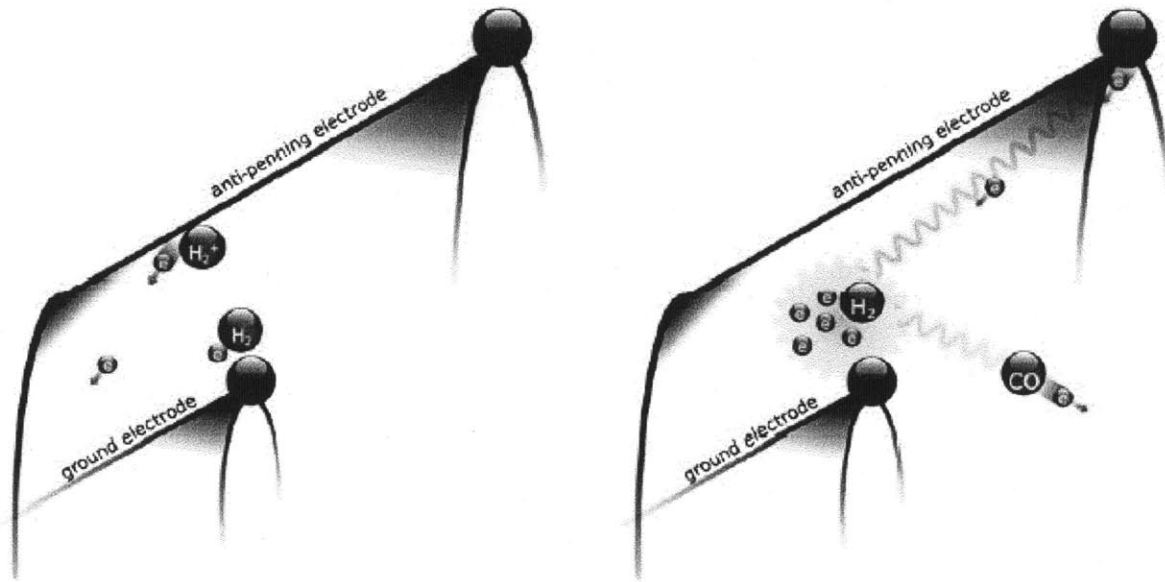
It was surprising to realize that Penning traps smaller than 100 cm^3 could produce background rates up to many kHz. To understand why this positive feedback effect occurred from secondary electrons, simulations of the pre-spectrometer were investigated. It turned out that positive ions produced did not cause secondary electrons to get caught in the Penning trap. The ions would go straight to the negative electrode. Secondary electrons produced would then follow the magnetic field lines straight to the ground electrode and away from the Penning trap.

The only other conclusion was that photons must produce this effect. It is intuitive that photons should be unaffected by the electromagnetic fields and will travel out in every direction. This allows for electrons all over to get created, where some can make it back to the Penning trap. Simulations confirmed this effect. Fig. 7.1.1 depicts the difference between the positive ions and the photons.

It was further shown through simulations that the Penning traps did not produce falsely detected secondary electrons, since they were located in positions where emitted electrons would never reach the detector. However, photons are bouncing all around on the inside of the spectrometer, which can then ionize and create secondary electrons. It was hypothesized and proven that these electrons were creating the background signal [4].

Simulations were able to show that the Penning trap causes ions and photons to be created, which then produce secondary electrons. However, only the photons create secondary electrons that re-enter the trap as well as electrons that can reach the detector. Now that simulations were able to determine how the Penning traps

Figure 7-1: The left image shows how positive ions create electrons that do not re-enter the Penning trap. The right hand side shows the contrary effect [4].



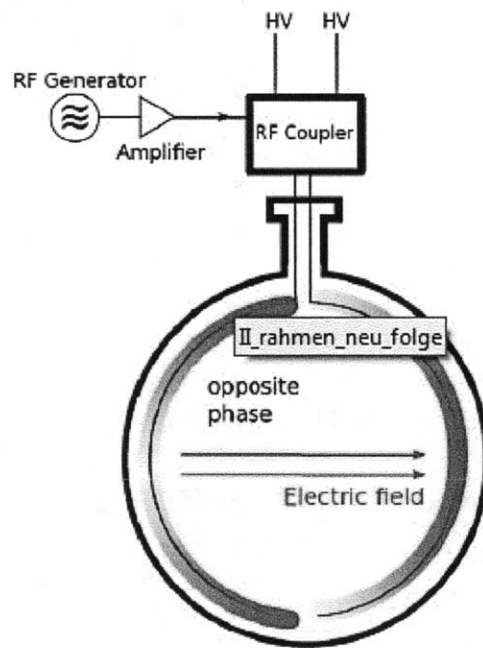
were creating background, removing the traps was investigated.

7.1.2 Electron Cyclotron Resonance Simulations

A technique called electron cyclotron resonance (ECR) was introduced to destroy the Penning traps. ECR applies an RF field pulse tuned to the cyclotron frequency of the trapped electrons. Fortunately, the cyclotron energy is approximately constant over the considered energy interval. The field is created by using a high frequency function generator, which is then amplified and coupled to electrodes to create an electric field. Fig. 7.1.2 shows the ECR setup.

The electric field creates stochastic heating, which disrupts the trap and can release the electron in less than 10 ms. If the trap is destroyed quickly, then photons never get created. Other trap removal mechanisms were designed, but ECR was chosen mainly for its speed. The electrons are sped up to over 100 keV, which causes the cyclotron radius to become larger than the main spectrometer. The detector cannot

Figure 7-2: The setup for ECR is displayed below. The frequency of the pulse generated must be tuned to be near the cyclotron frequency of the electrons in the Penning trap to ensure that they are excited [5].



collect data when the RF pulse is on. Fortunately, it takes about 10 minutes to build up secondary electrons, so the pulse is turned on and off every 10 minutes. [4].

Testing this with the pre-spectrometer showed that the background rate decreased by a half by introducing the ECR method [5]. However, the main spectrometer is larger than the pre-spectrometer and more complicated to model. While knowledge gained from simulating the pre-spectrometer has been applied to using ECR with the main spectrometer, no simulations have been performed to confirm and further explore this method. The derived surface integral formulation can be used to simulate the main spectrometer.

Physical data was obtained for the radio-frequency response of the main spectrometer. This can be used to compare to the new simulation of the main spectrometer. If the obtained measurements and the simulation agree, then the simulation can be used to find Penning traps. Over the summer, further analysis will be performed to see if ECR removes Penning traps in the main spectrometer. Ideally, simulation results will confirm that ECR can be applied to the main spectrometer to remove background data.

7.2 Conclusions

This thesis addresses the importance of removing Penning traps from KATRIN's spectrometers, which has been an issue in previous neutrino mass measurement experiments. For this reason, an extensive simulation of the spectrometer's response to electromagnetic pulses is studied. To do so, numerical methods must be introduced. Surface integral formulations were motivated, which allows for only the surface to be discretized to save memory. The desired surface integral equations were derived from Maxwell's equations, which resulted in introducing Green's functions to describe the generation of fields from currents. This direct derivation allows for very accurate results, since no approximations have been made to find the surface integral equations.

Once the surface integral equations were found, the method of moments was derived, which approximates the surface into discretized triangles and allows for a basis

function to be introduced. RWG basis functions were used for analyzing the sphere, however a face oriented basis was later developed for use with KATRIN. The MoM supplies a matrix equation, which was then solved using the Robin Hood method. This allows for the matrix to be inverted without ever being fully stored in memory. This allows for accurate solutions to be found for highly discretized systems.

This formulation can numerically solve electromagnetic scattering off of any geometry specified with a constant refractive index. This makes its application very broad, including antenna performance, plasmonic systems, and finding Penning traps in KATRIN's spectrometer. This surface integral formulation is truly a powerful numerical method.

Bibliography

- [1] “Katrin.” <http://en.wikipedia.org/wiki/KATRIN>, May 2012.
- [2] A. M. Kern and O. J. F. Martin, “Surface integral formulation for 3d simulations of plasmonic and high permittivity nanostructures,” *J. Opt. Soc. Am. A*, vol. 26, Apr 2009.
- [3] T. Hanninen and Sarvas, “Singularity subtraction integral formulae for surface integral equations with rwg, rooftop, and hybrid basis functions,” *Progress In Electromagnetics Research (PIER)*, vol. 63, pp. 243–278, 2006.
- [4] S. Mertens, *Study of Background Processes in the Electrostatic Spectrometers of the KATRIN Experiment*. PhD thesis, Institut für Experimentelle Kernphysik (EKP), Feb 2012.
- [5] Taken from a talk given by Benjamin Leiber in March 2012.
- [6] J. Angrik et al., “Katrin design report,” *Appl. Opt.*, vol. 7090, p. 245, 2004.
- [7] A. Goobar, S. Hannestad, E. Mortsell, and H. Tu, “A new bound on the neutrino mass from the sdss baryon acoustic peak,” *JCAP*, vol. 0606, p. 019, 2006.
- [8] M. Prall, “The katrin experiment and the pre-spectrometer at reduced retarding potential,” *Progress in Particle and Nuclear Physics*, vol. 66, no. 2, pp. 418 – 423, 2011. Particle and Nuclear Astrophysics International Workshop on Nuclear Physics, 32nd Course.
- [9] B. Flatt and J. Wolf, “Design of the katrin pre-spectrometer,” *Nuclear Physics B - Proceedings Supplements*, vol. 118, no. 0, p. 483, 2003. Proceedings of the XXth International Conference on Neutrino Physics and Astrophysics.
- [10] “The mac-e-filter.” <http://www-ik.fzk.de/tritium/em-design/index.html>, Feb 2006.
- [11] E. Balagurusamy, *Numerical Methods*. McGraw-Hill Education (India) Pvt Ltd, 1999.
- [12] J. Jin, *Theory and Computation of Electromagnetic Fields*. Wiley-IEEE Press, 2010.

- [13] I. Doležel, P. Karban, and P. Šolín, *Integral Methods in Low-Frequency Electromagnetics*. Wiley, 2009.
- [14] V. Chari and S. Salon, *Numerical Methods in Electromagnetism*. Electromagnetics Series, Academic Press, 2000.
- [15] R. F. Harrington, *Field Computation by Moment Methods*. Wiley-IEEE Press, 1993.
- [16] M. Gouda, *The Method of Moment for the Electromagnetic Scattering from Bodies of Revolution*. PhD thesis, University College of Borås, Sweden, 2008.
- [17] J. Kottmann and O. Martin, “Accurate solution of the volume integral equation for high-permittivity scatterers,” *Antennas and Propagation, IEEE Transactions on*, vol. 48, pp. 1719–1726, Nov 2000.
- [18] F. M. Kahnert, “Numerical methods in electromagnetic scattering theory,” *Journal of Quantitative Spectroscopy and Radiation Transfer*, vol. 79-80, pp. 775–824, 2003.
- [19] W. C. Chew, M. S. Tong, and B. Hu, *Integral Equation Methods for Electromagnetic and Elastic Waves*. Morgan & Claypool, 2009.
- [20] C. Tai, I. Antennas, P. Society, I. M. Theory, and T. Society, *Dyadic green functions in electromagnetic theory*. IEEE Press series on electromagnetic waves, IEEE Press, 1994.
- [21] W. C. Chew and Q. H. Liu, “Perfectly matched layers for elastodynamics: A new absorbing boundary condition,” *Journal of Computational Acoustics*, vol. 4, pp. 341–359, 1996.
- [22] S. Rao, D. Wilton, and A. Glisson, “Electromagnetic scattering by surfaces of arbitrary shape,” *IEEE Transactions on Antennas and Propagation*, vol. 30, no. 3, pp. 409–418, 1982.
- [23] P. Ylä-Oijala and M. Taskinen, “Calculation of cfe impedance matrix elements with rwg and n times;rwg functions,” *Antennas and Propagation, IEEE Transactions on*, vol. 51, pp. 1837–1846, aug. 2003.
- [24] W. Chew, *Waves and Fields in Inhomogeneous Media*. IEEE Press Series on Electromagnetic Waves, IEEE Press, 1999.
- [25] L. Råde and B. Westergren, *Mathematics Handbook For Science And Engineering*. Springer, 2004.
- [26] J. A. Formaggio, T. J. Corona, P. Lazić, and F. Gluck, “The robin hood method and its implementation,” *KATRIN*, Sep 2010.
- [27] M. Kerker, *The scattering of light, and other electromagnetic radiation*. Academic Press, 1969.

- [28] C. Bohren and D. Huffman, *Absorption and scattering of light by small particles*. Wiley, 1983.
- [29] W. J. Wiscombe, “Mie scattering calculations: Advances in technique and fast, vector-speed computer codes,” Jun 1979.
- [30] H. Du, “Mie-scattering calculation,” *Appl. Opt.*, vol. 43, pp. 1951–1956, Mar 2004.
- [31] C. Matzler, “Matlab functions for mie scattering and absorption,” Jun 2002.
- [32] D. Griffiths, *Introduction to Electrodynamics*. Prentice Hall, 1999.